An Odyssey in Exploring Nuclei: High-Precision Mass Measurements of Exotic Tin Isotopes and Progress Toward Implementing a Phase-Based Measurement Technique

by

Annabelle Isabella Czihaly
Bachelor of Science, University of the Fraser Valley, 2022

A Thesis Submitted in Partial Fulfillment of the
Requirements for the Degree of

MASTER OF SCIENCE

in the Department of Physics and Astronomy

An Odyssey in Exploring Nuclei: High-Precision Mass Measurements of Exotic Tin Isotopes and Progress Toward Implementing a Phase-Based Measurement Technique

by

Annabelle Isabella Czihaly
Bachelor of Science, University of the Fraser Valley, 2022

Supervisory Committee

Prof. A. A. Kwiatkowski, Co-Supervisor
(TRIUMF Physical Sciences Division; Department of Physics and Astronomy, University of Victoria)

Prof. M. Lefebvre, Co-Supervisor
(Department of Physics and Astronomy, University of Victoria)

Abstract

Precision mass measurements are integral in advancing our understanding of nuclear physics Since mass is a fundamental property of nuclei. TRIUMF's Ion Trap for Atomic and Nuclear science (TITAN) facility houses two high-precision mass spectrometers designed for mass measurements of radioactive isotopes: a Multiple-Reflection Time-of-Flight Mass Spectrometer (MR-TOF MS) and a Measurement Penning Trap (MPET).

This thesis presents the results from a MR-TOF MS campaign focused on the measurement of doubly magic ^{100}Sn where we successfully measured isotopes with mass numbers 104 through 107 to a precision of $\delta m/m \approx 10^{-7}$. Additionally, the most precise TITAN trap, MPET, is undergoing a major upgrade aimed at achieving precisions below $\delta m/m \approx 10^{-10}$. As part of this upgrade, a new phase-based measurement technique called Phase-Imaging Ion-Cyclotron-Resonance (PI-ICR) is being implemented. To support this implementation, the Phase-Imaging Analysis Tool (PhIAT) was upgraded to assist in system tuning and to perform mass measurements with PI-ICR.

Lay Summary

"Don't trust atoms, they make up everything!"

Atoms form the building blocks of the world around us, from the cells in our body to the universe we enjoy. Atoms themselves are made up of even smaller blocks, called subatomic particles, such as protons, neutrons, and electrons, with the number of protons and neutrons in an element specifying its atomic mass, A. The field of nuclear physics is devoted to understanding the nucleus, the core of an atom. In order to understand nuclei, we need to precisely know their fundamental properties, such as their mass and binding energy.

To this end, TRIUMF's Ion Trap for Atomic and Nuclear science (TITAN) is dedicated to performing precision mass measurements of radionuclides. This thesis presents the analysis and results of an experiment performed with TITAN to measure mass numbers $A = 104 - 107$ of tin, towards $A = 100$. Additionally, this thesis describes the upgrade and implementation of an analysis tool completed as part of the commissioning of an additional mass-measurement technique at TITAN. This body of work was completed with the goal of increasing the precision of future mass measurements at TRIUMF.

Preface

The research of this thesis was completed as part of the TITAN collaboration. Specifically,

- The group is lead by A. A. Kwiatkowski.
- The organization of the tin experiment was done by Pascal M. Reiter and Andrew Jacobs.
- The data collection of the tin experiment was performed by Soenke Beck, Eleanor Dunling, Jake Flowerdew, Danny Fusco, Leigh Graham, Zach Hockenbery, Chris Izzo, Andrew Jacobs, Brian Kootte, Yang Lan, Erich Leistenschneider, Eleni Marina Lykiardopoulou, Ish Mukul, Stefan F. Paul, Pascal M. Reiter and James L. Tracy, Jr.
- The analysis of the tin data was done by myself with guidance from Stefan F. Paul and Ali Mollaebrahimi.
- The implementation of PI-ICR at TITAN is in progress by myself, Mel Good, Sakshi Kakkar, and Dwaipayan Ray.
- The upgrade and testing of the Phase-Imaging Analysis Tool was completed by myself with guidance from William S. Porter.

The results of the tin experiment are highlighted in a publication, written and submitted by myself with contributing authors. The pre-print of the paper is available [1].

Table of Contents

List of Tables

List of Figures

Acknowledgements

Though this thesis is authored by one, the completion of this degree was not a solitary mission. In saying such, I extend my greatest thanks to those closest to me.

Mom and dad, thank you for your support, words of encouragement, and for always being a safe place for me to land. I cherish our family dinners and morning coffee talks. Thank you for getting me through this. To Bia, Lance, and Athena, thank you for always giving me helpful advice and bringing out the kid in me. To my partner, Zack, thank you for your patience and kindness. Your kind heart and efforts in supporting me through this process will always be remembered. To my friends, thank you for being kind shoulders to lean on and for bringing so much joy into my life.

I want to thank Drs. Jeff Chizma and Tim Cooper for without them, I would not be in graduate school. Tim, thank you for taking a chance on me in PHYS 112 all those years ago. Thank you for putting faith in me and supporting me in my academic journey. Jeff, before you, I never thought grad school was for me. I never even imagined it was an option! Your encouragement throughout my undergrad made me feel like I could actually do science. Thank you for your guidance over the years, I am forever thankful to have had you in my corner.

To my colleagues, particularly Ali, Sakshi, Sam, and Stefan, thank you for all your help and for never making me feel silly for asking some of my very, *very*, silly questions. You gave me a space to learn and supported me along the way and for that, I thank you dearly.

You have all empowered me to complete these projects and stay somewhat sane in the process. I am grateful to have you all in my life.

Lastly, I thank my supervisors, Drs. Ania Kwiatkowski and Michel Lefebvre. Ania, thank you for believing in me during my undergraduate degree by choosing me for my co-op in 2021. This placement changed the course of my academic journey and would not have been possible without your faith in me. Michel, thank you for your encouragement throughout my time with the University of Victoria and for always being willing to give me your input. Thank you both for all your support and guidance throughout my graduate degree.

May your courage guide your future

Dedication

Édesanyámnak és Édesapámnak.
Egy életen át hálás leszek nektek a bátorításotokért és az önfeláldozásotokért.
Kedves Szüleim, ezt a dolgozatot nektek ajánlom.

Chapter 1

Motivation

Atoms – the Lego of the Gods – form the building blocks of our Universe[1] and are named after the Greek word for "indivisible" or "uncuttable" (*Atomos*). At the heart of an atom is its nucleus, a collection of protons and neutrons. As atoms, and their nuclei, make up the world around us, it is in our best interest to understand their fundamental properties.

1.1 A Brief Jaunt into the Past: The Early Understandings of the Nucleus

As the history of physics is vast, this story will start at the beginning of the 20^{th} century. The year was 1904, just seven years after his discovery of the electron, and J. J. Thompson was again trying to understand the atom. He thought that electrons must be the building blocks of a larger entity and expected that they are surrounded by a sea of positive charge [2]; a model that was later dubbed the *plum pudding model* [2].

Shortly after, Hans Geiger and Ernest Marsden, fired alpha particles through metal sheets to investigate their paths [3]. They noticed that most of the alpha particles did not go directly through the foil as they would expect for a "pudding" of positive charge. Instead, some of the particles scattered in such a way that indicated one core as opposed to sea of charge, thus refuting the plum pudding model. This led to a landmark paper [4] in 1911 by Ernest Rutherford where he first defined the nucleus: the positively charged center of an atom. After this remarkable insight, the atomic revolution began. Antonius Johannes van den Broek proposed the atomic number Z (the net charge of a nucleus) [5]; Henry Mosely experimentally verified van den Broek's proposition [6]; and, Niels Bohr devised the atomic model of an atom [7]: a solar-system-like model with electrons orbiting the central nucleus in shells.

[1] As modern physics revealed, atoms themselves are made of subatomic particles, some of which are made up of even smaller, elementary particles. The further discussion of particle physics is left to other works.

The previous year, Walther Bothe and Herbert Becker noticed that when they fired alpha particles at a sample of beryllium, they were able to create a penetrating form of radiation [8]. This phenomena was further investigated by Irène Joliot-Curie and Frédéric Joliot-Curie [9], who discovered high-energy protons were created if this penetrating radiation was sent through a material containing hydrogen, increasing the ionization that they were able to detect. The next great revelation came in 1932 when James Chadwick determined that the radiation coming off the beryllium sheet had to be electrically neutral and have the approximate mass of a proton [9]. Finally, we had a formalism for the nucleus: the sum of the number of protons and neutrons.

Following the Bohr model of the atom came the liquid drop model of the nucleus [10]. Proposed by George Gamow in 1929, this model described the nucleus as a liquid drop, held together by the strong nuclear force. The mathematical expression of this model, the Semi-Empirical Mass Formula (SEMF) [11], combines theoretical explanations and experimental results to approximate the energy required to bind all particles inside the nucleus together, called the binding energy:

$$B(N,Z) = a_V A - a_S A^{2/3} - a_C \frac{Z(Z-1)}{A^{1/3}} - a_A \frac{(N-Z)^2}{A} + a_P \frac{1}{A^{1/2}} \tag{1.1}$$

where $B(N,Z)$ is the binding energy of an atom with Z number of protons and N number of neutrons, A the atomic number i.e. $A = Z + N$, a_V is the volume constant, a_S is the surface constant, a_C is the Coulomb constant, a_A is the asymmetry constant, and a_P is the pairing constant. This model explains the spherical shape and binding energy of most nuclei; however, it fails to explain, for example, the emergence of shell structure at particular occupation numbers of neutrons, as seen in Figure 1.1, and protons.

Two more scientists must be introduced to the story, Maria Goeppert Mayer and Hans Jensen. Independently from one another, they noticed the aforementioned discrepancies of the SEMF. They explained this phenomenon [13] by describing nucleons as occupying *shells* within a nucleus and subsequently earned the Nobel Prize in Physics in 1963 for their work. When a shell is fully occupied, it contains a magic[2] number of nucleons: 2, 8, 20, 28, 50, 82, and, in the case of neutrons, 126. This model successfully describes the emergence of shell structure that the SEMF could not predict (e.g. see Figure 1.1). However, in 1975, the first major failure of the shell model was published [14], wherein the authors concluded that the nuclear shell model was inconsistent with their experimental results, leading to the extinction of the $N = 20$ shell in sodium nuclides. Furthermore, the shell model has

[2]Ironically coined "magic" by Eugene Wigner to articulate his skepticism of the formulation.

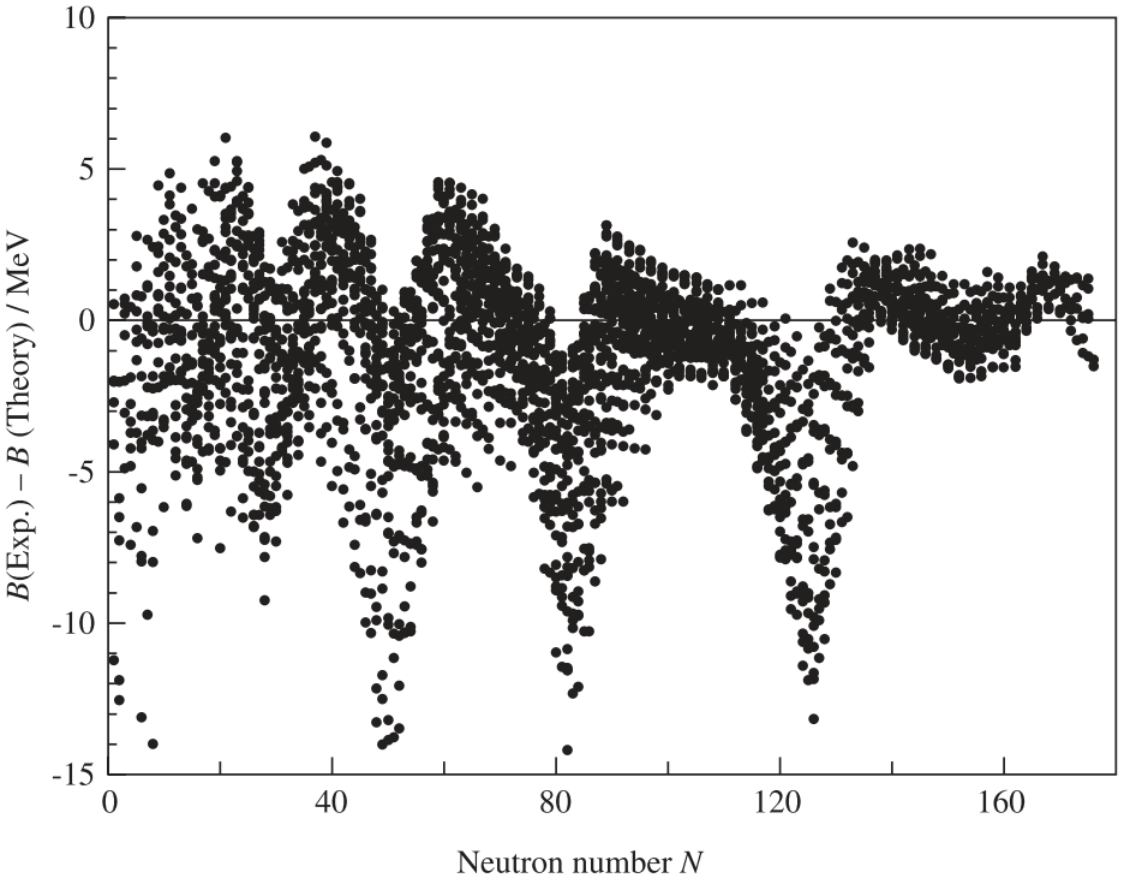

Figure 1.1: The difference in binding energy from the SEMF and experimental data as a function of neutron number. Notice repeating trends of large discrepancies around $N \approx 26, 50, 82, 126$. Taken from [12].

additional failures towards some dripline nuclei where there is a high asymmetry between the number of protons and neutrons. Full details on the evolution of shell structure can be found in [15]. These examples illustrate the need for additional models to describe nuclei.

Since the inception of Bohr's model of the atom, several theories to describe atoms and their nuclei have been developed (for a review of nuclear models, please refer to [16]). The most modern approach to describe nuclei is *ab-initio* nuclear theory [17], which attempts to "build nuclei from scratch" that is to say, to start from the beginning. This approach treats the nucleus as a collective system, as opposed to the individual particle approach of the Shell Model and, as a result, it is computationally taxing since it needs to account for all interactions of the many-body system. Current models treat nuclei as: non-interacting particles; complex, many-body systems; or a combination of the two. When comparing predictions to experimental data, there is general agreement for measured species though as

we veer towards regions that have not yet been experimentally determined, model predictions vary greatly. This highlights the need for more experimental data, with precision mass measurements being an integral component.

1.2 Why does mass matter?

The mass of an atom is defined as

$$m(N,Z) = Zm_p + Nm_n + Zm_e - B(N,Z)/c^2 \tag{1.2}$$

where N is the number of neutrons, Z is the number of protons, m_p and m_n are the masses of protons and neutrons, respectively, B is the binding energy, and c is the speed of light. As Table 1.1 presents, there are several applications of mass measurements.

Table 1.1: Fields of application and mass precision ($\delta m/m$) required for scientific impact. Adapted from [12].

Field	**Required Precision**
Chemistry	$10^{-5} - 10^{-6}$
Nuclear structure (e.g. shells, halos, deformation)	$10^{-6} - 10^{-8}$
Nuclear astrophysics (e.g. r-process, rp-process)	10^{-7}
Nuclear models	$10^{-7} - 10^{-8}$
Weak interaction studies (e.g. CKM unitarity)	10^{-8}
Fundamental constants	$\leq 10^{-10}$

As mass measurements directly probe the binding energy of nuclei, precision measurements can reveal particular trends in the nuclear structure such as unexpected or disappearing magic numbers. To investigate the shell structure of nuclei, it is helpful to calculate the two-neutron separation energy, S_{2N}, the energy required to remove two neutrons from a nucleus. Two-neutron separation is preferred over single-neutron separation as it smooths out staggering from open and closed orbitals. As seen in Figure 1.2, the two-neutron separation energy generally decreases as N increases and steeply drops at magic numbers. This phenomena of steep drop-offs can be understood by the energy levels above a shell gap where it requires less energy to remove the first two neutrons [18].

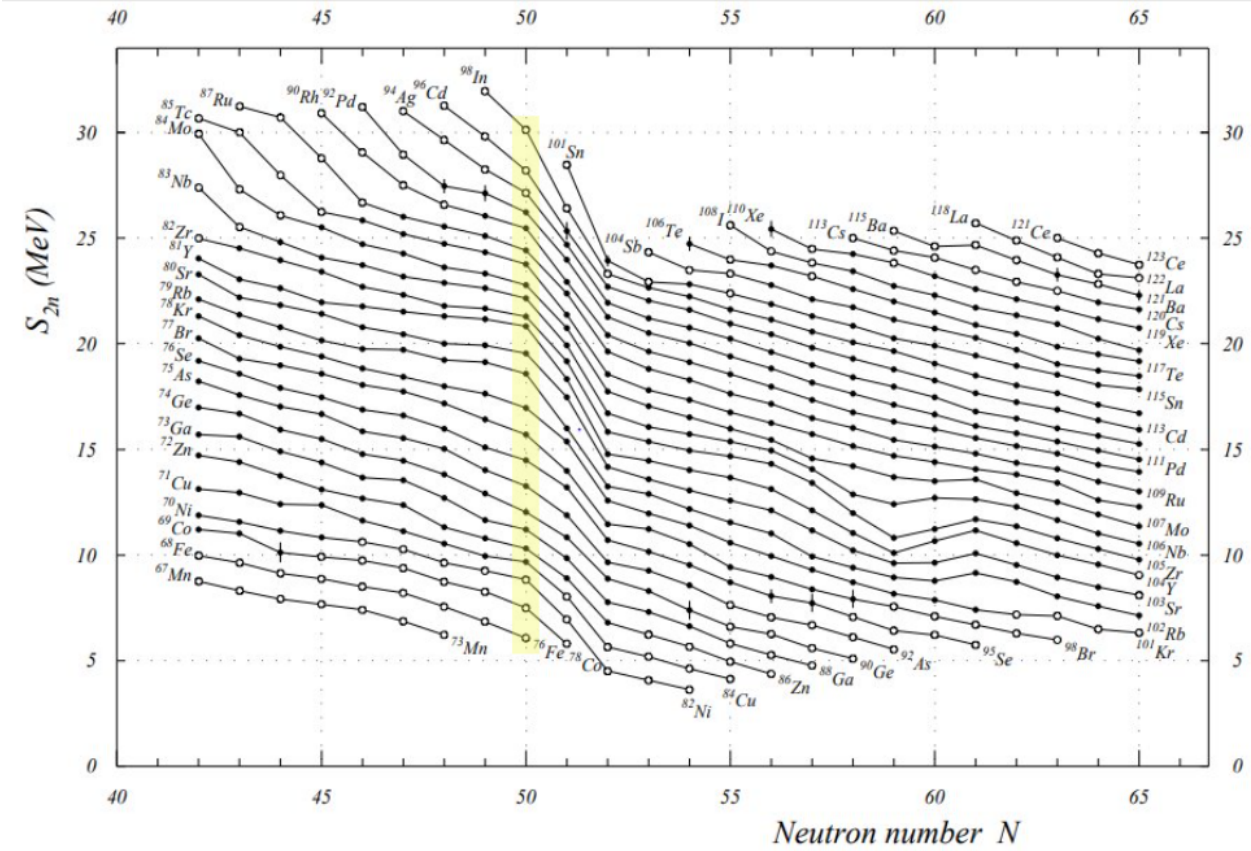

Figure 1.2: Two-neutron separation energy S_{2n} as a function of neutron number for $N = 42-65$. Coloured in dots represent measurements whereas hollow circles indicate extrapolated values. There is a general trend of decreasing two-neutron separation energy as the number of neutrons increase. Furthermore, we see a steep drop off at the magic number $N = 50$, highlighted in yellow, which is indicative of a fully occupied shell. Additionally, we see irregular line shapes of Nb, Zr, Y, and Sr in the $\approx N = 59 - 61$ region, due to deformation [16]. Taken from [19].

Furthermore, investigations of S_{2N} can provide signs of the deformation of nuclei. Nuclei are typically assumed to be spherical; however, deformed ground-state nuclei have different energy level structure which affects their binding energy [16]. This can be visually seen in S_{2N} plots, such as in the $\approx N = 59 - 61$ region of Figure 1.2.

Precision mass measurements also play a role in the study of nuclear halos [18]; nuclei which have loosely bound neutrons which create a "halo" surrounding the core of the nucleus. Proton halos are possible though less common due to the Coulomb barrier [18]. This effect can be seen in neutron-rich light nuclei approaching the neutron dripline [20] since the valence neutron (or pair of neutrons) have low separation energies, characteristic of dripline nuclei and due to the short range of the nuclear force [20]. The result of this halo effect

causes neutrons to be found at distances significantly beyond the typical nuclear radius [21]. Separation energies can be probed with precision mass spectrometry such as at TRIUMF's Ion Trap for Atomic and Nuclear science (TITAN) facility [22].

Furthermore, mass measurements serve as a crucial link between the experimental observations and theoretical predictions within the framework of the Standard Model of particle physics. Among its most stringent tests is the unitarity of the Cabibbo–Kobayashi–Maskawa (CKM) matrix [23] which describes the mixing of quarks via the weak interaction. The most constrained test of the unitarity of this matrix is the top row:

$$|V_{\mathrm{ud}}|^2 + |V_{\mathrm{us}}|^2 + |V_{\mathrm{ub}}|^2 = 1 + \Delta_{\mathrm{CKM}} \tag{1.3}$$

with $\Delta_{\mathrm{CKM}} = 0$ satisfying the condition of a unitary matrix as demanded by the Standard Model. In this equation, $|V_{\mathrm{ud}}|^2$, $|V_{\mathrm{us}}|^2$, and $|V_{\mathrm{ub}}|^2$ represent the probabilities of a transition from one flavour of quark to another flavour; for example, V_{ud} is the matrix element corresponding to the probability that an up quark transitions to a down quark. Investigating $|V_{\mathrm{ud}}|$ is of particular interest, since it has the greatest contribution at about 97%. For pure Fermi β decays, $|V_{\mathrm{ud}}|$ can be expressed as [23]

$$|V_{\mathrm{ud}}|^2 = \frac{K}{2G_V^2 Ft(1+\Delta)} \tag{1.4}$$

where K is a constant, G_V is the vector-coupling constant, Ft is the corrected strength of the transition, and Δ is a transition-independent correction factor. These particular decays are known as superallowed β-decays meaning that the nuclear states before and after the decay have the same parity *and* spin i.e. $0^+ \rightarrow 0^+$. The determination of Ft requires precise knowledge of the half-life, branching ratio, and end-point energy, Q, of the Fermi decay [23]. The Q-value is defined as the energy released or absorbed during a nuclear reaction and as such, requires knowledge of the mass of the parent and daughter nuclei present in the reaction. High-precision mass spectrometry determines these Q-values by precision measurements of masses; since F depends on the Q-value raised to the fifth power, they must be determined with sub-keV precision [23], which is well within grasp for measurements performed with Penning trap mass spectrometers. As of a 2020 review [23], 15 of the listed 23 Ft values have been determined to a precision of at least 0.23% due to advancements in experimental techniques, which resulted in greater achievable precision; however, eight Ft values out of this list remain to be fully characterized [23]. This underscores the need for more Q-value, half-life, and branching ratio determinations to verify previous findings and investigate additional

Ft values, since there are at least 23 transitions known or predicted to exist [23].

1.3 Techniques in Mass Spectrometry

J. J. Thompson's work laid the ground for mass spectrometry by showing that electric and magnetic fields can alter the trajectory of charged particles. His student, Francis Aston, is regarded to have created the first mass spectrometer. Using parallel magnetic and electric fields, he accelerated ions, deflected them, and detected their trajectories using a photographic plate. His work revealed the presence of isotopes for every element and eventually led to the development of his whole number rule: the mass of an isotope can be described by (whole) multiples of the mass of a hydrogen atom [24]. Furthermore, he deduced that isotopes of the same element are approximately equal in weight. These extraordinary insights and discoveries led to him being awarded the Nobel Prize in Chemistry in 1922 [25]. The innovative idea of using electromagnetic fields to manipulate ions was revolutionary and continues to be the backbone in contemporary mass spectrometry.

By utilizing electric and magnetic fields, we are able to confine and manipulate charged particles. Furthermore, by exploiting known trapping parameters, we can determine the frequency or time of flight, and therefore the mass, of ions with high precision. The masses of stable and exotic species of nuclides are typically determined using two main techniques: those based on the time of flight of an ion and those based on the frequency of its motion when stored or trapped.

1.3.1 Storage-Ring Mass Spectrometry

Storage-ring mass spectrometry is based on the measurement of a particle's revolution frequency or time in a storage ring [26]. The revolution frequency, f, or revolution time, T, is determined via

$$\frac{\Delta f}{f} = -\frac{\Delta T}{T} = -\frac{1}{\gamma_t^2}\frac{\Delta(m/q)}{m/q} + \frac{\Delta v}{v}\left(1 - \frac{\gamma^2}{\gamma_t^2}\right) \tag{1.5}$$

where m/q is the mass-to-charge ratio, v is the velocity, γ is the relativistic Lorentz factor[3], and γ_t is the transition γ, which corresponds to the transition point of a storage ring, a constant that is determined by the optics of the ring [26]. Therefore, the revolution frequency or time of particles is directly related to their mass-to-charge ratios.

There are two methods that have been developed for storage-ring mass spectrometry, Schottky (SMS) and Isochronous (IMS) [26]. SMS is based on the frequency analysis of

[3] $\gamma = 1/\sqrt{1 - \frac{v^2}{c^2}}$ where c is the speed of light.

Schottky noise. Noise is detected by pick-up electrodes in the beam path, with each stored ion inducing a signal. This process produces a spectrum of lines at each harmonic of the revolution frequency and since particles of different masses will bend around the ring with different radii, they will travel different orbits, and thus make unique peaks within the spectra. SMS minimizes Δv by means of electron cooling so that all particles have the same mean particle velocity. Alternatively, the condition for isochronicity demanded by IMS is $\gamma = \gamma_t$; that is, the revolution frequency is independent from velocity. This is accomplished by adjusting ion optics so that the velocity difference between particles of the same species is counteracted by adjusting orbital paths [26].

Storage-ring mass spectrometry has several benefits, namely the simultaneous measurement of multiple species in varied charge states, the ability to handle nuclides with short half-lives, and single-ion sensitivity. A downside of this technique is the large footprint required; for example, the experimental storage ring at GSI in Germany is $\approx$ 108 m in circumference [27]! For further reading regarding storage rings, please refer to [26].

1.3.2 Bρ Time-of-Flight Mass Spectrometry

The Bρ TOF technique for mass spectrometry is based on the motion of a charged particle through a dipole-based magnetic system, with magnetic rigidity Bρ [28] where B and ρ is the magnetic field strength and radius of curvature of the path, respectively. The mass of a non-relativistic ion is then determined via

$$\frac{m}{q} = \frac{B\rho}{v} = B\rho\frac{t}{L} \tag{1.6}$$

where m is the mass of the ion of interest, q is the charge of the ion of interest, t is the time of flight of the ion, and L is the path length that the ion traverses. Since m can be expressed as $m = \gamma m_0$, this equation is rewritten as

$$B\rho = \frac{\gamma m_0}{q}\left(\frac{L}{t}\right) \tag{1.7}$$

where γ is the relativistic Lorentz factor and m_0 is the rest mass. Since the magnetic rigidity of a system is difficult to precisely determine, Bρ TOF requires the measurement of several reference ions to calibrate the ratios between the rigidity, mass, and velocity [28]. This technique can achieve precisions on the order of $\delta m/m \sim 10^{-6}$, and since measurement times are short ($< 1\mu$s), nuclides with short half-lives can be explored with ease [28].

Bρ TOF and storage-ring methods are capable of handling half-lives down to $\sim \mu$s how-

ever, a significant drawback of both techniques is their complexity and physical footprint; both require large experimental facilities, and BρTOF requires multiple calibrating masses that are simultaneously measured with radioactive ion beam [28]. Furthermore, both techniques achieve precisions lower than that of other methods as are discussed below.

1.3.3 Mutiple-Reflection Time-of-Flight Mass Spectrometry

Multiple-Reflection Time-of-Flight Mass Spectrometry (MR-TOF MS) technique boasts resolving powers of $m/\Delta m \sim 10^5$ and precisions of $\delta m/m \sim 10^{-7}$ [29]. Since the precision of time-of-flight-based techniques scales with the path length, a longer path is ideal. A practical way of increasing the path length is by the use of electrostatic ion mirrors to "bounce" ions several hundred times, creating flight paths of hundreds of meters in a compact, ≈ 0.5 meter-long apparatus. Here, electrostatic beam elements are used instead of, for example, magnetic optics used in Bρ TOF and storage-ring methods. This is due to the lower energy regime (e.g. the TITAN MR-TOF MS typically receives a beam energy of ~ 1.3 keV) where electrostatic beam elements are better suited. This is in contrast to, for example, the higher energy regime (~ 300 MeV/u experimental energy) at experimental storage ring at GSI [27] where magnetic optics are utilized.

One advantage of the MR-TOF MS method, when compared to Bρ TOF, is that one of two calibrants can be calibrated off-line i.e. with a stable ion, instead of several on-line calibrant ions. Additionally, the solution for the mass of ions in this technique is quite simple to determine since the solution is in the form of a quadratic [29]. The achievable precision permits studies of, for example, the shell structure within nuclei and nuclear astrophysical processes, although is insufficient for studies of the weak interaction [12]. Thus, the need for a more precise technique is achieved through Penning Trap Mass Spectrometry (PTMS).

1.3.4 Penning Trap Mass Spectrometry

The first Penning trap was developed by Hans Dehmelt in the 1950s; and in 1989, he was awarded a portion of the Nobel Prize in Physics for his contributions [30]. A Penning trap uses a strong magnetic field and a weak electrostatic field to trap ions in three dimensions. By utilizing a magnetic field of strength B, the mass m of ions with a particular charge q, can be precisely determined from the measurement of the cyclotron frequency, ν_c, as understood from

$$\nu_c = \frac{qB}{2\pi m} \,. \tag{1.8}$$

With PTMS, precision up to $\delta m/m \sim 10^{-10}$ is attainable for radionuclides and beyond for the study of stable species [18]. When ions are in the trap, they exhibit three eigenmotions: reduced cyclotron, magnetron, and axial motion [18], as seen in Figure 1.3. In order to

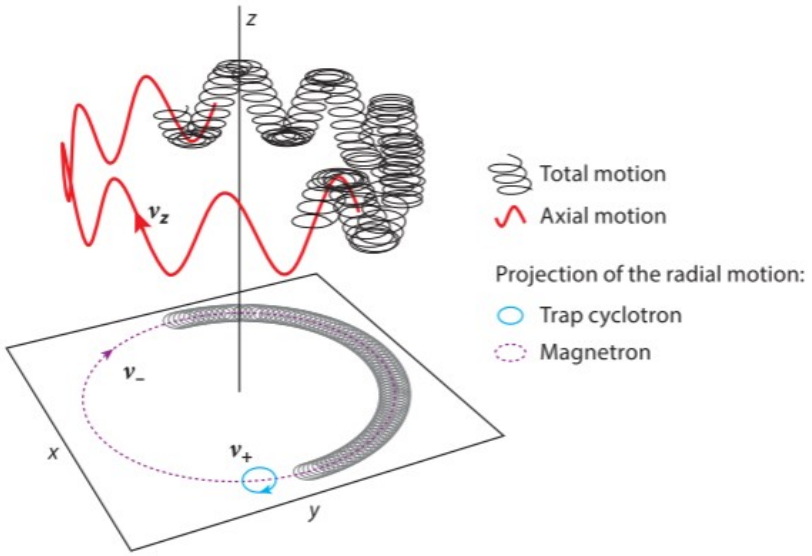

Figure 1.3: Schematic depicting the three eigenmotions of an ion in a Penning trap. The black line represents the sum of all motions, the red line represents the axial motion, and the xy plane shows the projection of the two radial motions: magnetron (purple dotted) and reduced cyclotron (cyan). Taken from [18].

amplify or minimize an eigenmotion of a particular frequency, excitations can be applied. For example, when a dipole excitation is applied at a frequency equal to that of the reduced cyclotron, magnetron, or axial frequency, the corresponding motion is excited. Alternatively, if a quadrupolar excitation of a specific frequency is applied, the motion of ions is fully converted from e.g. reduced cyclotron motion to magnetron motion, and vice versa. For further detail about excitations and the manipulation of ions, please refer to Chapter 4.

For the study of exotic nuclides, there are two primary techniques for determining cyclotron frequency, Time-of-Flight Ion Cyclotron Resonance (TOF-ICR) [31] and a newer technique, Phase-Imaging Ion Cyclotron Resonance (PI-ICR) [32].

In the TOF-ICR technique, the TOF of an ion is measured from the trap to the detector through the magnetic field gradient, which is a function of the magnetic field inside the trap, radial and axial energy of the ion, and electric and magnetic potentials along the path [18]. A quadrupolar radio frequency excitation is applied, and since this excitation effects the orbital magnetic moment of ions, the TOF is also altered. Once this process is repeated for various

frequencies, a plot of the TOF versus excitation frequency, a resonance, is created. From this resonance, the mass can be deduced. Utilizing the TOF-ICR technique, the TITAN group was able to measure the mass of $^{11}Li^{+}$ [33] which has a half-life of just 8.8 ms, securing the world record for a Penning trap measurement of a nuclide with such a short half-life! The major disadvantage of this technique is that it requires ≥ 50 ions to perform a measurement [18]. Moreover, the precision of this technique is Fourier limited by the duration of the excitation and hence, the half-life [12].

In 2012, an alternate technique for mass measurement, PI-ICR, was developed [32]. In this method, the radial motion of an ion is mapped on a position-sensitive detector, after a period of excitation-free evolution, t_{acc}. The study of how the phase, ϕ_c, evolves gives the mass of the ions which can be understood from [32]

$$\nu_c = \frac{\phi_c + 2\pi N(t_{\text{acc}})}{2\pi t_{\text{acc}}} \tag{1.9}$$

where ν_c is the cyclotron frequency and $N(t_{\text{acc}})$ are the number of revolutions completed in time t_{acc}. This technique offers a five-fold gain in precision and a 40-fold gain in resolving power when compared to TOF-ICR for singly charged ions [32]. The latter portion of this thesis presents the work towards implementing the PI-ICR technique at TITAN which promises to increase precision to $\delta m/m \sim 10^{-10}$.

To conclude, there are several techniques for mass spectrometry, each with their own unique advantages and shortcomings, as briefly summarized in Table 1.2.

Table 1.2: Brief summary comparing and contrasting various methods of mass spectrometry, with more detail provided in text. Since various nuclear physics investigations require different mass precisions in order for the work to be of scientific impact (as presented in Table 1.1), differing techniques are advantageous. Information sourced from [12, 18, 26, 28].

Method	$\sim \boldsymbol{\delta m/m}$	$\boldsymbol{T_{1/2}} \gtrsim$	**Advantages**	**Disadvantages**
Bρ TOF	$10^{-5} - 10^{-6}$	1 μs	Broadband; single-ion sensitivity; low background	Multi-mass calibrations; large physical footprint
Storage rings: SMS	$10^{-6} - 10^{-7}$	1 s	Broadband; single-ion sensitivity	Large physical footprint; half-life limited due to cooling time
Storage rings: IMS	10^{-5}	1 μs	Broadband; single-ion sensitivity	Large physical footprint; isochronous condition must be uniquely tuned
MR-TOF MS	$10^{-6} - 10^{-7}$	1 ms	Broadband; single-ion sensitivity; large dynamic range	Requires one isobaric calibrant; prone to adverse effects from ion-ion interactions
PTMS: TOF-ICR	$10^{-7} - 10^{-9}$	3 ms	Robust technique; less prone to systematic errors; requires only one stable calibrant mass	Fourier limited precision; requires $\geq$ 50 ions for precision; prone to adverse effects from ion-ion interactions
PTMS: PI-ICR	10^{-10}	3 ms	Only needs two ions for measurement	Requires prior knowledge about ion; prone to adverse effects from ion-ion interactions; precise optical requirements

1.4 This Work

In this work, I present the analysis and results of a MR-TOF MS measurement of $^{104-107}$Sn (Chapter 3). Additionally, I present the principles of Penning trap mass spectrometry (Chapter 4) and discuss the developments towards the implementation of PI-ICR, including an on-line analysis suite (Chapter 5).

Chapter 2

TITAN Overview

The experimental work for this thesis was conducted in Vancouver, British Columbia, Canada with TRIUMF's Ion Trap for Atomic and Nuclear science (TITAN) facility [22]. Since 2007, the TITAN facility has conducted many high-precision mass measurements of exotic nuclei probing nuclear structure, nuclear astrophysics, and physics beyond the Standard Model.

This chapter provides an overview of the facility, seen in Figure 2.1, which includes a Radio Frequency Quadrupole (RFQ) for cooling and bunching beam, a Multiple-Reflection Time-of-Flight Mass Spectrometer (MR-TOF MS) which is capable of both performing mass measurements and acting as a beam purifier for the downstream traps, an Electron Beam Ion Trap (EBIT) for charge breeding singly charged ions (SCI) to highly charged ions (HCI), and the Measurement Penning Trap (MPET) for precision mass measurements of radionuclides. Additionally, this chapter provides a brief overview of radionuclide production at TRIUMF.

2.1 Radionuclide Production at TRIUMF's Isotope Separator and ACcelerator

Radioactive ion beams at TRIUMF are created with the Isotope Separator and ACcelerator (ISAC) using the Isotope Separation On-Line (ISOL) method [34] in which a primary beam impinges on a target that is made of a specific material in order to illicit a particular outcome. The most common target materials at TRIUMF are uranium carbide, silicon carbide, and tantalum. The material of the target is chosen depending on the desired reaction products created, their diffusion rates out of the target, and the power the targets can tolerate without degrading. Nuclear reactions in the target, mostly spallation, fragmentation, and, for uranium carbide targets, fission, create radionuclides that then diffuse out of the $\approx 2000^{\circ}$C target, which can be subsequently ionized by one of four ion sources (surface ion source [35], ion guide laser ion source [36], resonance ionization laser ion source [37], and

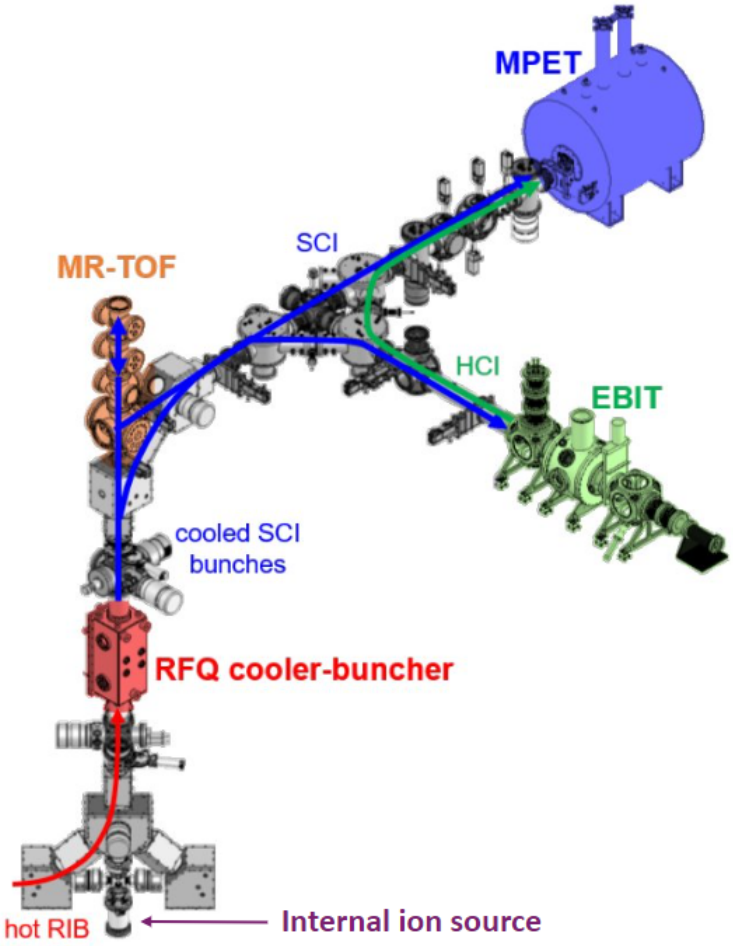

Figure 2.1: Overview of the TITAN facility. The blue and green lines indicate the path of singly charged ions (SCI) and highly charged ions (HCI), respectively. Beam from ISAC (red line) or the internal TITAN ion source (indicated in purple) travel to the RFQ. The helium-gas-filled RFQ cools and bunches beam using segmented electrodes and delivers ion bunches to the downstream traps. The MR-TOF MS reflects ions hundreds of times between a pair of electrostatic mirror electrodes to perform mass measurements. The EBIT traps and creates highly charge ions by means of electron bombardment. Finally, the MPET uses a strong magnetic field and weak electric field to trap ions and determine masses with high precision. In the experimental work for this thesis, the RFQ, MR-TOF, and MPET were used.

forced electron beam induced arc discharge [38]). The ion source is chosen to best match the species of interest with each source having unique advantages and disadvantages. For example, the forced electron beam induced arc discharge source ionizes noble gasses, which cannot be ionized via surface or laser ionization (due to their high ionization energy). Full details on the TRIUMF ion sources can be found in [35, 36, 37, 38]. The radioactive ion

beams are then transported to various research stations, such as TITAN.

At TRIUMF, the primary beam is created in the cyclotron by accelerating negatively charged hydrogen. TRIUMF's cyclotron is composed of a radio frequency field and a magnetic field. Since the radio frequency field accelerates ions by repeatedly switching polarity and the magnetic field confines ions in the transverse plane, the ions spiral outwards towards the outer edge of the cyclotron. Then, the beam collides with a small foil [39] that strips the beam of its bound electrons, leaving a high-energy proton beam to be deflected and steered toward the ISAC target to produce a radioactive ion beam.

2.2 Cooling and Bunching Beam with the Radio Frequency Quadrupole

The RFQ [40] cools and bunches incoming beam from ISAC or TITAN's ion source for delivery to the rest of TITAN. Since the measurement traps perform poorly with continuous beam [40], the RFQ is necessary to bunch the incoming beam. Furthermore, cooling is required to minimize the energy distribution of the incoming beam and match the beam energy to the acceptance [40] of the rest of the TITAN traps. Cooling is accomplished by successive collisions with a light and inert gas, helium. With each subsequent collision with the gas, the kinetic energy of the beam decreases, thus decreasing the temperature of the beam (as $E \propto T$) until it reaches equilibrium with the surrounding gas. To impede beam dispersion, a radial force is created by applying a radio frequency field to four, one-meter long circular rods arranged in a quadrupolar configuration. An electrostatic gradient transfers the ions into the bunching region, where the beam is accumulated and then extracted by pulsing the electrodes surrounding the bunch. A schematic of this process can be seen in Figure 2.2. Full details on the TITAN RFQ can be found in [40].

2.3 Multiple-Reflection Time-of-Flight Mass Spectrometer

Commissioned in 2017 [41, 42], the MR-TOF MS is the newest of the TITAN traps. The design is based off of the MR-TOF MS at GSI [43, 44, 45] and was built in collaboration with the Justus Liebig University Giessen, Germany. In this technique, the flight time of ions over a long path length created by a pair of electrostatic mirrors is measured. The MR-TOF MS at TITAN can be used as a mass-based beam purifier with the purified beam being sent to the EBIT and/or MPET, or it can be used as a standalone device for mass measurements.

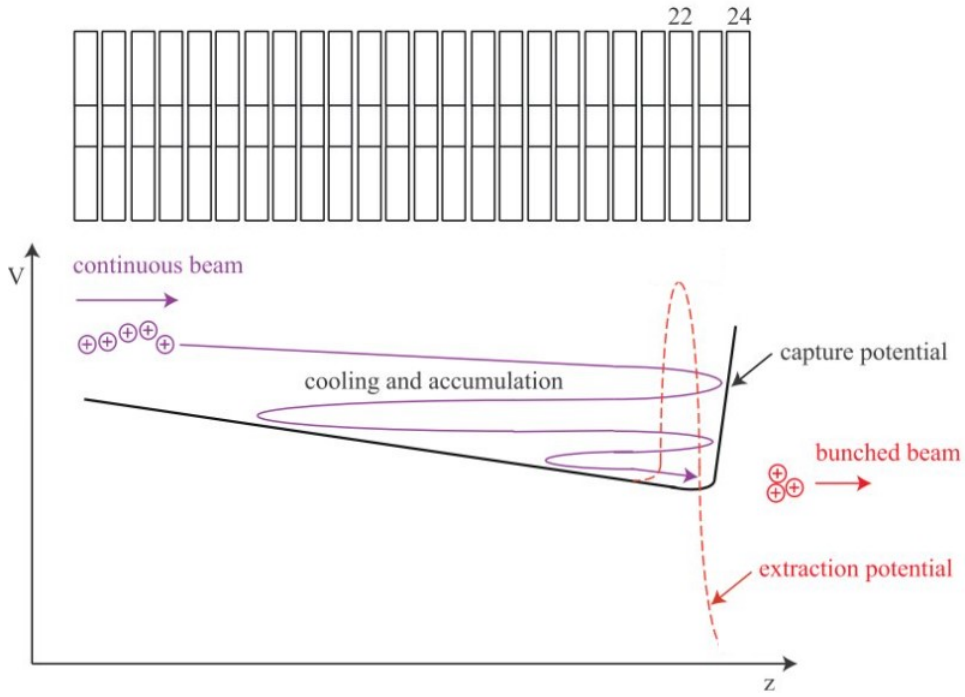

Figure 2.2: Schematic of the segmented electrode structure of the RFQ (top) and RFQ operation (bottom). Of the 24-electrode structure of the RFQ, electrodes 22 and 24 have been highlighted since they are used for applying the pulse to eject ions from the bunching region. The purple line shows the accumulation process; the black line shows the capture potential; and, the red dashed line shows the trapping and extraction potentials. Adapted from [40].

2.3.1 Time-of-Flight Mass Spectrometry

Multiple-reflection time-of-flight mass spectrometry is governed by simple, non-relativistic kinematics i.e. $E_{\text{kin}} = \frac{1}{2}mv^2$. In words, ions with the same kinetic energy but different masses will have different speeds and, thus, different times of flight over a given path. Experiencing a potential U, ions with charge q will accelerate and have kinetic energy of $E_{\text{kin}} = qU$. The time of flight (TOF), t_{TOF}, of the ions is

$$t_{TOF} = L\sqrt{\frac{m}{2E_{\text{kin}}}} \tag{2.1}$$

with L being the flight path, m being the mass of an ion, and $E_{\text{kin}} = qU$ being the kinetic energy of ions. By inspection, $t_{\text{TOF}} \propto \sqrt{m/q}$. The resolving power R is given by

$$R = \frac{m}{\Delta m} = \frac{t_{\text{TOF}}}{2\Delta t} \tag{2.2}$$

where Δt is the time spread of the ions. From this equation, we can see that by increasing the TOF while minimizing Δt, we can increase the resolving power of our system. By Equation 2.1, we can see that this can be accomplished by increasing the flight path, L. In an MR-TOF MS, this is done in a compact way by folding the flight path by means of a pair of ion mirrors separated by a drift tube. The electrostatic mirrors enable ions to reflect hundreds of times, effectively creating a path length of several hundred meters in a device no longer than about one meter. In order to temporally separate species and perform precision measurements, a resolving power of $R \geq 10^5$ is needed.

2.3.2 Apparatus

The TITAN MR-TOF MS is composed of main two sections: a preparation portion and a mass analyzer, as seen in Figure 2.3. These sections are discussed below.

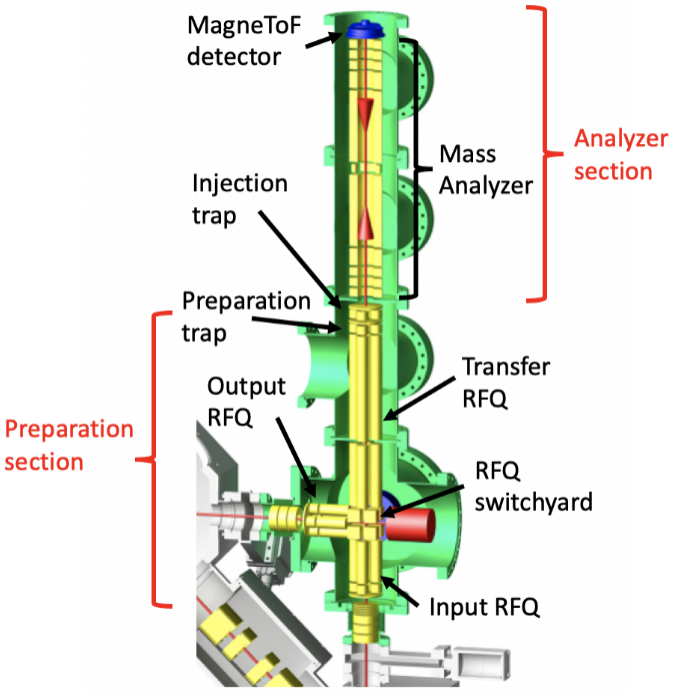

Figure 2.3: Schematic of TITAN MR-TOF MS. The preparation section is composed of a series of RFQs and the analyzer section includes the mass analyzer (where the ions travel and reflect) and detector.

Preparation

The preparation section of the MR-TOF MS receives beam from the TITAN RFQ and optimizes the beam prior to injection into the mass analyzer. The preparation section is composed of several RFQs that operate similarly to the TITAN RFQ discussed in Chapter 2. The RFQs of the MR-TOF are:

1. Input RFQ: Receives beam from the TITAN RFQ
2. RFQ switchyard
    - Directs beam to the MR-TOF to operate for different operational modes i.e. as a mass separator or a mass measurement device
    - Allows for beam merging with the MR-TOF internal ion source
3. Output RFQ: Sends the beam to EBIT or MPET
4. Transfer RFQ: Transports beam from the switchyard to the mass analyzer

Mass Analyzer

The mass analyzer is where ions "bounce" between a pair of electrostatic mirrors until reaching sufficient mass-to-charge separation over a long flight path. The mass analyzer, seen in Figure 2.4, is made of nine primary electrodes: four mirror electrodes on each side separated by a drift tube. The purpose of the drift tube is to maintain the kinetic energy of ion bunches after their exit from the RFQ [29] and to provide the flying region to the ions. Additionally, contained in the middle of the drift tube is the Mass Range Selector (MRS), an electrostatic deflector. The MRS can be switched between transmission and deflection modes to preserve ions of interest while deflecting impurities [46]. The inner most electrodes (E4 and E6 in Figure 2.4) are focusing lenses that minimize beam spread and the outer most electrodes (E1-3 and E7-9 in Figure 2.4) create the electrostatic mirrors from which, when a potential is applied, the ions bounce off. From the analyzer, ions can be sent to the MagneTOF detector for TOF measurement or be sent to EBIT and/or MPET via the MR-TOF RFQ switchyard.

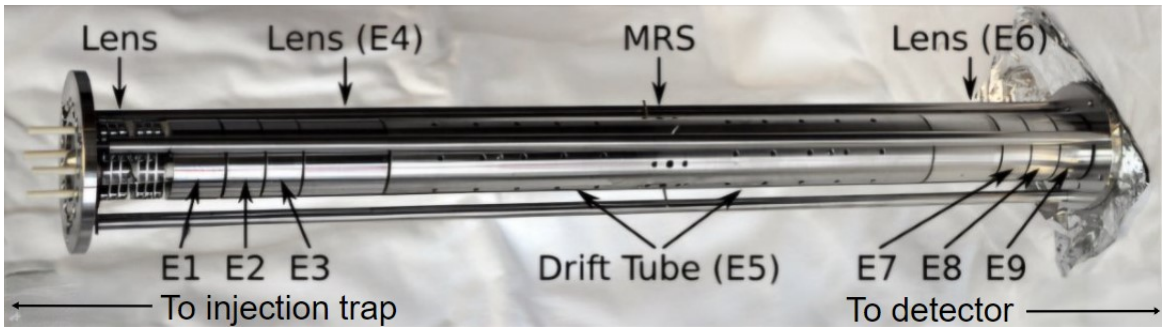

Figure 2.4: TITAN MR-TOF MS mass analyzer with significant elements labeled. Adapted from [47].

2.3.3 Mass-Selective Re-Trapping

Mass-selective re-trapping [48] is a unique feature of the TITAN-Giessen MR-TOF design that enables isobaric cleaning. After being trapped in the injection trap, ions are injected to the mass analyzer. After completing a number of turns for sufficient mass separation, ions of interest are dynamically re-captured in the injection trap by switching the (injection) trap from a retarding potential to a trapping potential [49]. In doing so, only ions of interest (IOI) are re-captured. Ions are sent back into the analyzer, fly through, and are detected. A schematic of this operation can be seen in Figure 2.5.

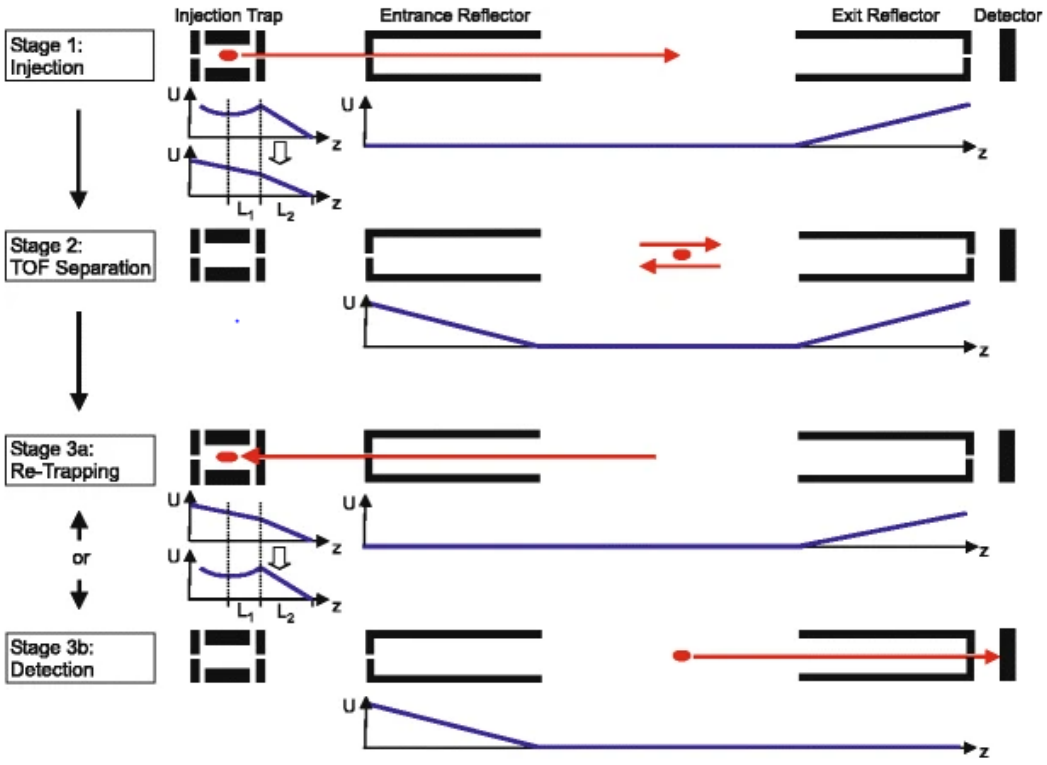

Figure 2.5: Schematic of re-trapping in the TITAN MR-TOF. Ions are first prepared in the injection trap and are subsequently injected into the analyzer. After temporal separation, ions of interest are dynamically re-trapped in the injection trap while contaminant ions remain in the analyzer to be electrostatically deflected, removing most contaminants from the system. Then, the ions of interest are re-injected into the analyzer and fly through, directly to the detector. Taken from [49].

Mass-selective re-trapping suppresses contaminants and permits a dynamic range (the ratio of the IOI to contaminants) as large as $1 : 10^8$ [48]. In the tin experiment, re-trapping reduced the maximum ratio of IOI to contamination from about $1 : 10^2$ to (at most) $1 : 30$. Furthermore, the use of re-trapping allows the MR-TOF MS to achieve sensitivities of rates as low as 0.0007 detected ions per second [50].

2.4 Electron Beam Ion Trap

The EBIT is a charge breeder that removes electrons by successive electron impact [22]. It is made up by an electron gun, drift tubes (inside a superconducting magnet), and an electron collector. The superconducting magnet and electron beam are responsible for trapping ions radially, with axial confinement provided by electrostatic potentials on the drift tubes [51]. An electron beam removes their electrons and, thus, increases their charge state. The

resulting highly charged ions can then be transported to MPET for mass measurement to improve the achievable precision. The EBIT was not used in this thesis work.

2.5 Measurement Penning Trap

The MPET relies on the confinement of ions in the presence of a strong magnetic field and weak electrostatic field. In the presence of a uniform magnetic field, $\vec{B}$, ions of charge q will experience a force $\vec{F}$ governed by

$$\vec{F} = q\vec{v} \times \vec{B} \tag{2.3}$$

where $\vec{v}$ is the velocity. This confines the ions and causes them to orbit in the plane perpendicular to $\vec{B}$ with angular frequency, ω_c, given by

$$\omega_c = \frac{qB}{m} \tag{2.4}$$

where m is the mass of the ion. By superimposing an electrostatic field, we can confine ions in all three spatial dimensions. By measuring the frequency and knowing q and $\vec{B}$, the mass can be determined. The ideal field is defined by a ring electrode and two end cap electrodes to form a quasi-infinite hyperboloid of revolution, as seen in Figure 2.6. In this configuration,

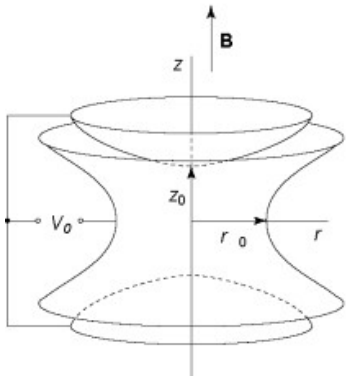

Figure 2.6: Hyperbolic Penning trap, highlighting characteristic dimensions of the trap, r_0 and z_0, the magnetic field $\vec{B}$, and the applied potential V_0. Taken from [52].

an electric potential of the form

$$V(r,z) = \frac{V_0}{4d_0^2}(2z^2 - r^2) \tag{2.5}$$

is created, where V_0 is the trapping voltage, $d_0 = \sqrt{z_0^2/2 + r_0^2/4}$ is the characteristic dimension of the trap, and z_0 and r_0 are the axial and radial coordinates, respectively (with respect

to the z axis). This field provides axial confinement of ions with radial confinement provided by a strong, 3.7 T magnetic field. While the electric field perturbs the ion motion from pure cyclotron motion, as will be derived in Chapter 4, one can still directly measure the trap-cyclotron frequency and, thus, the mass via the techniques introduced in Section 1.3.4.

MPET measurements based on TOF-ICR have reached a precision as low as 5×10^{-9} [53]. Furthermore, the MPET can achieve the highest resolving power and $\delta m/m$ of the TITAN traps and boasts the world record for fastest measurement [33]. By combining PTMS with HCI produced in the EBIT, the $\delta m/m$ can be further enhanced [22] (charge breeding can also be used for beam purification and secondary production [54]). This can be understood from [51]

$$\frac{\delta m}{m} \propto \frac{m}{qBT_{RF}\sqrt{N}} \tag{2.6}$$

where m, q, and N are the mass, charge, and number of ions respectively, T_{RF} is the excitation time, and B is the magnetic field strength. The combination of RIB, HCI, and PTMS is uniquely leveraged at TITAN. Recent upgrades include making the trap cryogenic to improve storage of HCI and implementing the phase-based technique to boost precision. As part of this implementation, an analysis tool was created that was upgraded for the TITAN system and tested. A full discussion of this tool is provided in Chapter 5.

Chapter 3

MR-TOF Mass Measurements of Tin Approaching Doubly Magic $^{100}_{50}Sn_{50}$

3.1 Experimental Procedure

The tin isotopes for this work [1] were created by impinging a proton beam current of 55 μA on a thick tantalum target. Fragmentation and spallation reactions in the target created radionuclides which then diffused out of the target. The tin isotopes were then ionized by TRILIS [55] in a three-step resonant laser scheme. This process excites a valence electron, causing the tin to become ionized. The beam was then sent through a dipole magnet separator, with a resolving power of approximately 2500 [56], eliminating any non-isobaric species. The RIB was then transported to TITAN's helium-gas-filled RFQ ion trap [40] to be cooled and bunched with bunches sent to the MR-TOF MS. In the MR-TOF MS analyzer, a dynamic time focus shift (TFS) was done to align the bunch's time focus with the downstream detector to maximize the temporal resolution. Each subsequent turn after the first TFS turn is an isochronous turn (IT). For this experiment, the ions underwent between 385 and 398 ITs in order to best separate the tin ions from isobaric contaminants. Thereafter, the ions were ejected from the analyzer by opening the ion mirror closest to the detector where an ETP MagneTOF™ measured the time of flight (TOF) of the ions.

To reduce contamination, ions were mass-selectively re-trapped (see Figure 2.5) [48]. Once ions were temporally separated in the analyzer, the ions of interest were re-trapped in the injection trap while the contaminants were deflected. The ions from the injection trap were re-cooled and re-injected into the analyzer, completed another TFS and more ITs, and were ejected toward the detector. Along with the ion of interest (IOI), tin, the delivered beam contained contaminants. The primary contaminants were identified as atomic In^+, Pd^+, and Ag^+ as well as molecular $Zr^{16}O^+$, $Sr^{19}F^+$, and $Y^{16}O^+$. All species were identified based

on isotopic patterns based on their presence across the spectra collected, with unambiguous identification of tin done with measurements with TRILIS lasers on and off. When the lasers are off, ionization of tin is prevented resulting in significantly lower yields or no tin present, which can be seen in Panel B of Figure 3.1. Alternatively, when lasers are on, tin is able to be ionized and as a result, is visible in the spectra, as seen in Panel A of Figure 3.1.

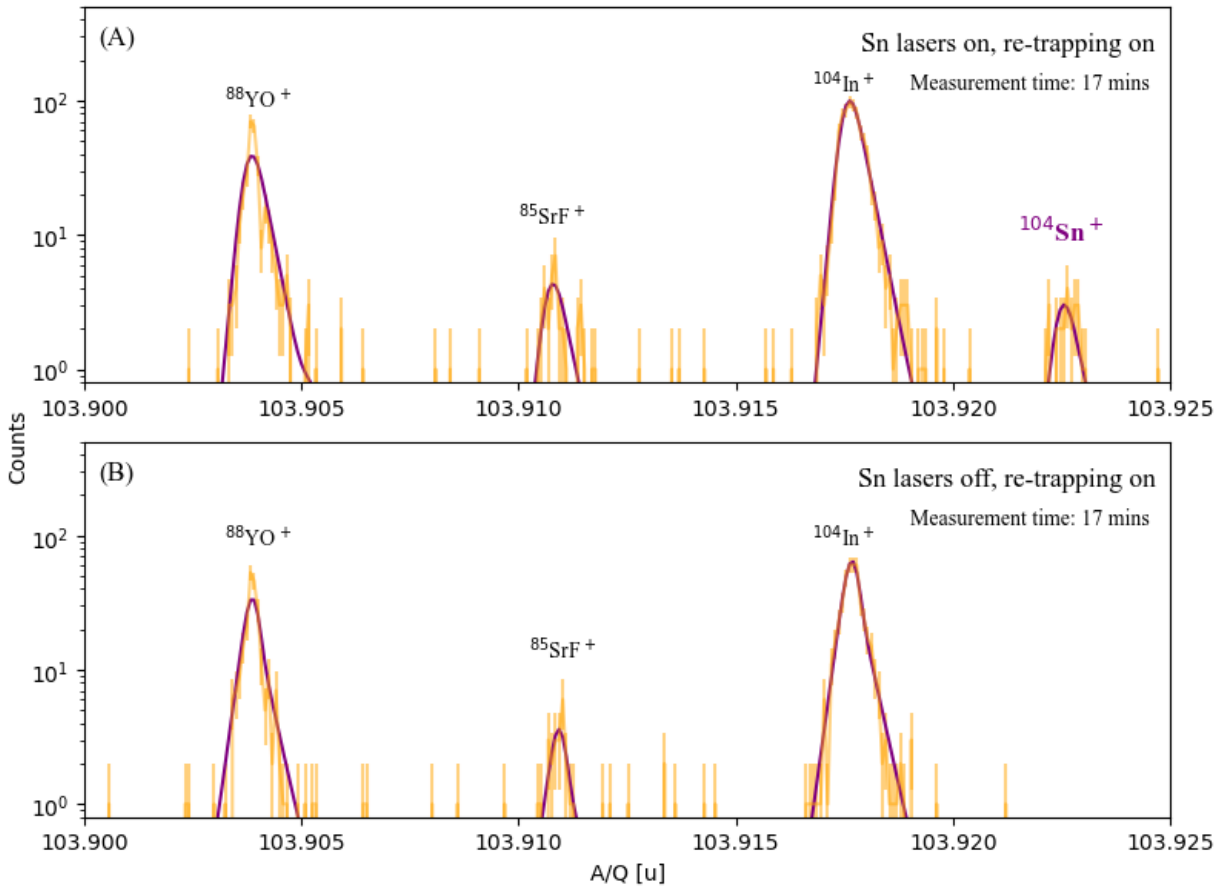

Figure 3.1: Spectra showing the effects of tin-ionizing laser beams (unblocked: Panel A; blocked: Panel B) at $A/Q = 104$, where $Q = q/e \equiv$ charge state. Comparing spectra identifies the tin.

In the experiment, we successfully measured $^{104-107}$Sn, enabling investigations of shell structure in the neighbourhood approaching doubly magic ^{100}Sn. Moreover, due to the broadband capability of this technique, we also measured ^{89}Zr and ^{90,91}Y, marking the first direct mass measurements of these nuclides.

3.2 Data Analysis

The data analysis follows the procedure described in [46] and is performed in two stages. First, TOF Control software [57] is used to convert the TOF spectrum collected to a mass-to-charge spectrum via

$$\frac{m}{q} = \frac{c \cdot (t - t_0)^2}{(1 + N_{IT} \cdot b)} \tag{3.1}$$

where m and q are the mass and charge of the ion, respectively, t is the TOF of the ion, t_0 is the delay between the starting signal and the true start of ions (due to electronic processing and signal speed in cables), c and b being calibration parameters, and N_{IT} being the number of ITs. Device-specific parameters c and t_0 were determined prior to the experiment with well-known $^{133}Cs^+$ from the MR-TOF MS thermal ion source. For the determination of b, a time-resolved calibration (TRC) [46] is done using a high-statistics reference peak which corrects drifts in the time-of-flight spectra caused by, for example, diurnal temperature cycles in the experimental hall. TRCs further improve the achievable resolving power and, therefore, the separation of the IOI from the contamination inherent to RIB production. A TRC splits a given spectrum into calibration blocks and determines the calibration parameter, b, for each block, by fitting a high-statistics reference peak to a Gaussian distribution. The effects on a spectra before and after a TRC is performed can be seen in Figure 3.2. For this analysis, the TRC calibrants were $Y^{16}O^+$ for $A/Q = 104, 105$ and $Zr^{16}O^+$ for $A/Q = 106, 107$, where $Q = q/e \equiv$ charge state. TRC calibrants were chosen based on each spectra: for example, in the mass spectra for $A/Q = 106, 107$, ZrO^+ was better resolved or had more statistics when compared to YO^+ and therefore, was a better choice to be the TRC calibrant. Additionally, since $^{90}Y^+$ and $^{91}Y^+$ became ions of interest after the experiment, they were not selected as TRC calibrants for $A/Q = 106, 107$ as this would have skewed the results.

The next step of the analysis is the fitting procedure. The fitting procedure is done using hyper-Exponentially Modified Gaussian (hyper-EMG) probability density functions, packaged together in a compact analysis program [46]. Hyper-EMGs are Gaussian functions with varying exponential tails on either side, given as [46]:

$$h_{\text{EMG}}(x; \mu, \sigma, \Theta, \eta_-, \tau_-, \eta_+, \tau_+) = \Theta h_{-\text{EMG}}(x; \mu, \sigma, \eta_-, \tau_-) + (1 - \Theta) h_{+\text{EMG}}(x; \mu, \sigma, \eta_+, \tau_+) \tag{3.2}$$

where $h_{\pm\text{EMG}}$ are defined as

$$h_{\pm\text{EMG}}(x; \mu, \sigma, \nu_\pm, \tau_\pm) = \sum_{i=1}^{N_\pm} \frac{\eta_{\pm i}}{2\tau_{\pm i}} \exp\left[\left(\frac{\sigma}{\sqrt{2}\tau_{\pm i}}\right)^2 \pm \frac{x - \mu}{\sqrt{2}\tau_{\pm i}}\right] \text{erfc}\left(\frac{\sigma}{\sqrt{2}\tau_{\pm i}} \pm \frac{x - \mu}{\sqrt{2}\sigma}\right) \tag{3.3}$$

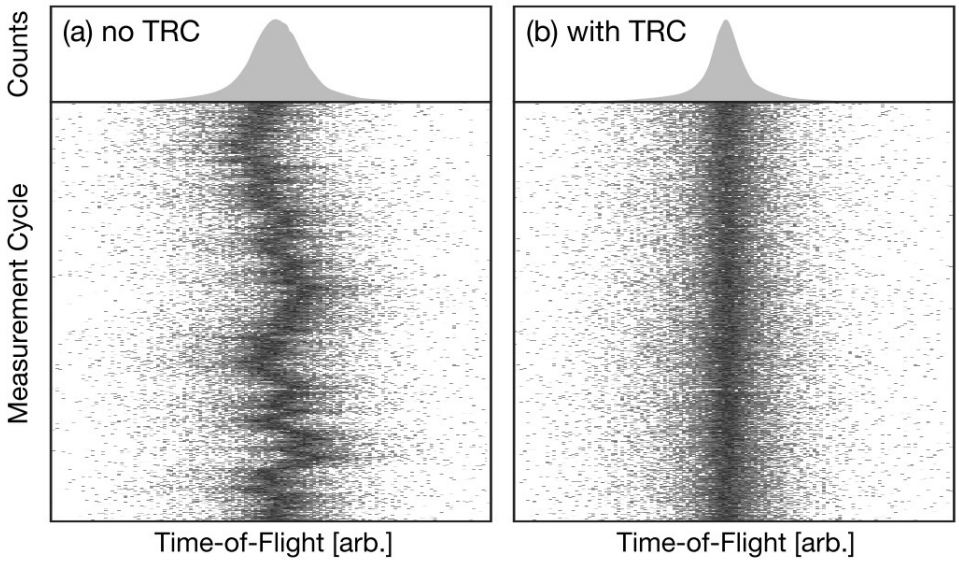

Figure 3.2: Example of a spectra before and after a TRC. The top panels represent the total counts. As we can see on the right hand side (Panel B), when a TRC is performed, the jitter and drifts present on the left (Panel A) is smoothed out and as a result, the peaks become sharper, as shown re-summed on the top panel. Taken from [58].

with Θ as the mixing weight for determining the contribution of the left and right tails, $N_{\pm}$ being the negative and positive tail order (left is negative, right is positive), $\mu = \mu_g$ (the parameter that determines the specific mass-to-charge values) and $\sigma = \sigma_g$ being the mean and standard deviation of the Gaussian distribution, respectively, $\tau_{\pm}$ being the decay constants of the exponential tails, and $\eta_{\pm}$ being the tail weights [59].

All parameters are found by fitting hyper-EMGs to an isolated peak with high statistics, known as the shape calibrant. Fits of the shape calibrant are done by minimizing Pearson's *chi-squared statistic*, defined as

$$\chi^2_P = \sum_i \frac{(f(x_i) - y_i)^2}{f(x_i) + \epsilon} \tag{3.4}$$

where x_i is the center of the i-th bin, y_i are the counts contained in the i-th bin, and $\epsilon = 10^{-10}$ is included for "numerical robustness" [59] as $f(x_i)$ nears zero. Then, all peaks in the spectra are fit with the Poisson maximum likelihood estimator (MLE) method, defined as

$$L = 2\sum_i \left[f(x_i) - y_i + y_i \ln\left(\frac{y_i}{f(x_i)}\right)\right]. \tag{3.5}$$

The last step of the analysis procedure is to determine the mass values via

$$m_{\mathrm{IOI}} = \frac{\mu_{\mathrm{G,\ IOI}}}{\mu_{\mathrm{G,\ cal}}}(m_{\mathrm{cal}} - Q_{\mathrm{cal}}m_e) + Q_{\mathrm{IOI}}m_e \tag{3.6}$$

where m_{IOI} is the mass of the IOI, $\mu_{\mathrm{G,\ IOI}}$ and $\mu_{\mathrm{G,\ cal}}$ are the peak centers of the IOI and calibrant, respectively, m_{cal} is the mass of the calibrant taken from the latest AME (here, AME 2020 [60] was used), Q_{IOI} and Q_{cal} are the charge states of the IOI and calibrant, respectively, and m_e is the mass of an electron. The mass calibrant was chosen by selecting a high-statistics, well-known peak that is well separated from other peaks in each spectra. The mass calibrants used for this analysis are specified in Table 3.1 in the column labeled *Mass Calibrant*.

3.3 Fit Results

Using the analysis procedure described above, analysis was completed for $A/Q = 104 - 107$ and are presented below.

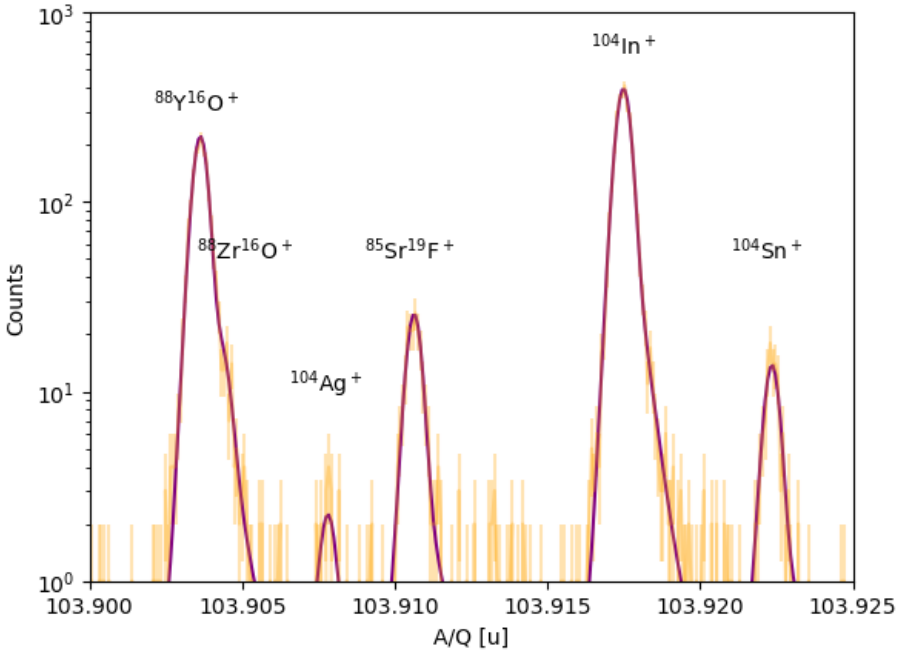

Figure 3.3: EMG fit results of $A/Q = 104$. The dominating contaminants are isobaric $^{104}In^+$ and molecular $^{88}Y^{16}O^+$. This spectra and the subsequent fit was created by merging two data files with identical settings (a routine procedure) to simplify the analysis. The calibrants chosen for analysis are: $^{88}Zr^{16}O^+$ (TRC and mass calibrant) and $^{104}In^+$ (shape calibrant).

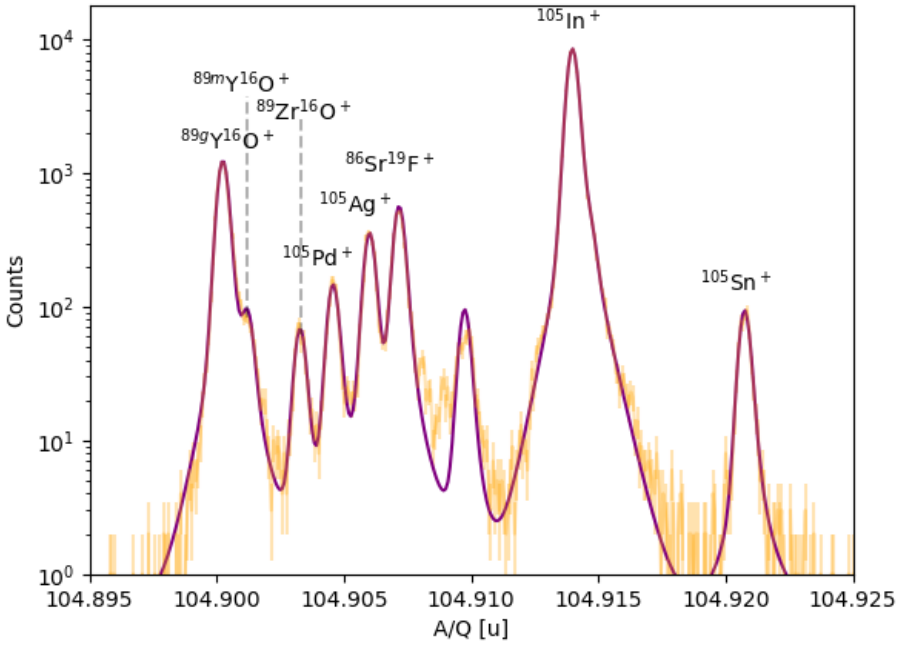

Figure 3.4: EMG fit results of $A/Q = 105$. The dominating contaminants are isobaric $^{105}In^+$ and molecular $^{89}Y^{16}O^+$. This spectra and the subsequent fit was created by merging two data files with identical settings (a routine procedure) to simplify the analysis. The calibrants chosen for analysis are: $^{89}Zr^{16}O^+$ (TRC and mass calibrant) and $^{105}In^+$ (shape calibrant).

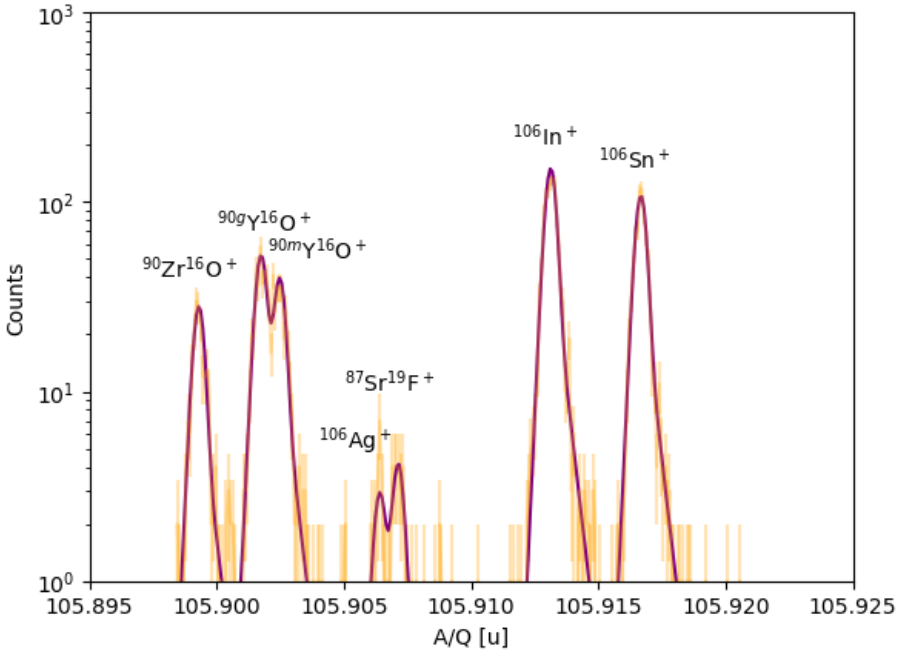

Figure 3.5: EMG fit results of $A/Q = 106$. The calibrants chosen for analysis are: $Zr^{16}O^+$ (TRC and mass calibrant) and $^{106}In^+$ (shape calibrant).

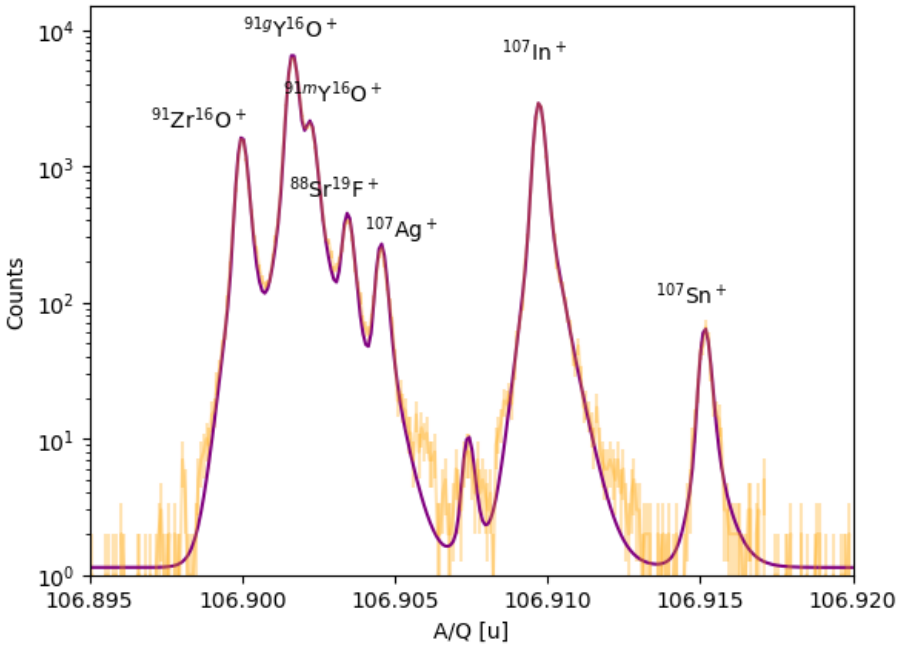

Figure 3.6: EMG fit results of $A/Q = 107$. The calibrants chosen for analysis are: $^{91}Zr^{16}O^+$ (TRC and mass calibrant) and $^{107}In^+$ (shape calibrant).

3.4 Uncertainty Contributions

The main sources of uncertainty in measurements [46] come from statistical uncertainty, peak-shape uncertainty, calibrant uncertainty, and non-ideal ejection uncertainty. The total error is the sum of these sources in quadrature i.e.

$$\sigma_{\text{total}} = \sqrt{\sigma_{\text{stat}}^2 + \sigma_{\text{sys}}^2} \tag{3.7}$$

where σ_{stat} and σ_{sys} are the uncertainties from statistics and systematics, respectively, where

$$\sigma_{\text{stat}} = \sqrt{\sigma_{\text{EMG}}^2 + \sigma_{\text{PS}}^2 + \sigma_{\text{cal}}^2} \tag{3.8}$$

$$\sigma_{\text{sys}} = \sqrt{\sigma_{\text{NIE}}^2} \tag{3.9}$$

where EMG, PS, cal, and NIE subscripts are the error contributions from hyper-EMG, peak shape, calibrant, and non-ideal ejection, respectively. Each uncertainty contribution is discussed below.

3.4.1 Statistical Uncertainties

Exponentially Modified Gaussian

The statistical uncertainty from a weighted maximum likelihood estimator (wMLE) is given by [46]

$$\sigma_{\mathrm{EMG}} = A_{\mathrm{stat}} \frac{\mathrm{FWHM}}{\sqrt{N_{\mathrm{counts}}}} \tag{3.10}$$

where a value of $A_{\mathrm{stat}} = 0.53 \pm 0.02$ is typical [46], FWHM is the full width at half maximum, and N are the number of counts. To determine A_{stat}, samples of a well-isolated reference peak are selected from the data, and synthetic spectra are created and fit using wMLE. The standard deviation of the area and peak centroids are determined and used to quantify A_{stat}. Full details on this procedure can be found in [46].

Peak Shape

The uncertainty of the peak shape, σ_{PS}, is found by changing each fitting parameter $(\mu, \sigma, \Theta, \nu_{\pm}, \tau_{\pm})$ of the model by its uncertainty and refitting all peaks in a given spectra [46]. The change in the mass-to-charge ratio is determined and taken as the uncertainty of the peak-shape parameter. Then, these peak-shape uncertainties are added together in quadrature to determine the final peak shape uncertainty value.

Calibrant

The uncertainty of the calibrant, σ_{cal}, includes the statistical uncertainty of the peak (described above) and the uncertainty of the evaluated mass value [60] of the calibrant.

3.4.2 Systematic Uncertainties

Systematic uncertainties are dominated by Non-Ideal Ejection (NIE). Full details on the sources of systematic error contributions can be found in [46]. NIE was quantified by completing a scan of the opening time of the second mirror (closest to the detector) and measuring the TOF of $^{133}Cs^{+}$ after one turn in the analyzer against different opening times. As this process is not instantaneous and some ringing occurs within the second mirror, the electric potential the ions experience as they fly towards the detector can be altered thus affecting the TOF. A histogram of the TOF data was generated and fit with a Gaussian distribution, with the FWHM of the distribution corresponding to time via $\delta t = \mathrm{FWHM}$. Then, the

systematic uncertainty of the mirror opening time was determined from

$$\sigma_{\mathrm{NIE}} = \frac{\delta m}{m} = 2\frac{\delta t}{t} = 2\frac{\mathrm{FWHM}}{t} \quad . \tag{3.11}$$

As determined from the second mirror opening time scan, FWHM= 5.7847×10^{-4} s and $t = 0.01$ s. From this, the total systematic error was determined as an upper limit [61] to be

$$\sigma_{\mathrm{sys}} = 3.0 \times 10^{-7}. \tag{3.12}$$

3.5 Results

The results of the experiment and data analysis are presented in Table 3.1 and are compared to the latest Atomic Mass Evaluation (AME 2020) [60]. Additionally, deviations between literature and the results of this analysis are shown in Figure 3.7.

Table 3.1: Summary of the mass excess values determined in this work and comparison to AME 2020 [60]. Number of detected events, calibrant species, and ionic mass ratios are presented. All ions were singly charged.

Nuclide	Number of Events	Ionic Mass Ratio	Mass Calibrant	$\mathrm{ME_{TITAN}}$ (keV)	$\mathrm{ME_{AME}}$ (keV)	Difference (keV)
^{89}Zr*	448	1.00002898	^{89}Y^{16}O	-84883(35)	-84878(3)	-5.2(35)
^{90g}Y*	370	1.000023135	^{90}Zr^{16}O	-86498(40)	-86497(0.4)	-0.6(40)
^{90m}Y*	266	1.000030123	^{90}Zr^{16}O	-85805(41)	-85815(0.4)	10(41)
^{91g}Y*	36797	1.000015435	^{90}Zr^{91}O	-86351(33)	-86351(2)	0.7(33)
^{91m}Y*	9328	1.000021048	^{90}Zr^{16}O	-85797(35)	-85796(2)	-1(35)
^{104}Sn	101	1.00018007	^{88}Y^{16}O	-71601(50)	-71627(6)	26(50)
^{105}Sn	626	1.000195519	^{89}Y^{16}O	-73349(34)	-73338(4)	-11(34)
^{106}Sn	776	1.000164119	^{90}Zr^{16}O	-77327(37)	-77354(5)	26(37)
^{107}Sn	350	1.000141815	^{91}Zr^{16}O	-78511(34)	-78512(5)	1(34)

*For ^{A}Y and ^{A}Zr, since they were measured as oxides, the ratio is the ionic mass of the molecule of interest divided by the ionic mass of the molecular calibrant (e.g. $\mathrm{m_{^{89}Zr^{16}O^{+}}}$ / $\mathrm{m_{^{89}Y^{16}O^{+}}}$).

^{104}Sn: The mass excess of ^{104}Sn published in AME 2020 is a weighted average from that of a Penning-trap measurement performed at JYFLTRAP [62] and indirect Q-value decay measurements [64, 65] for total value of −71627(6) keV. The result of this analysis gives a mass excess of −71601(50) keV, a 26 keV difference from that reported in the AME.

^{105}Sn: The mass excess of ^{105}Sn published in AME 2020 is presented as a weighted average between two Penning-trap mass measurements performed at JYFLTRAP [62] and SHIPTRAP [63] with an averaged value of −73338(3) keV. The result of this analysis gives a

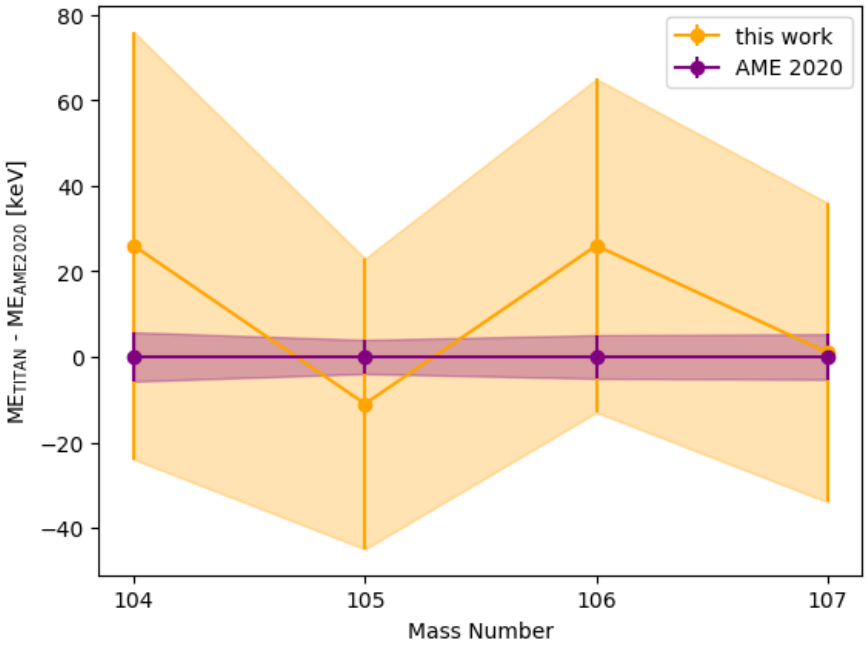

Figure 3.7: Deviation of tin isotopes from AME 2020 [60]. This work is presented in orange and AME 2020 values are represented in purple, with bands representing errors. The data for this experiment was collected in a mere four hours and shows excellent agreement with the literature results. The error bars obtained in this work ($\leq$ 50 keV) are sufficient to make conclusions about the structure of nuclei, in a fraction of the time when compared to the literature values which were obtained via PTMS [62, 63].

mass excess of −73349(34) keV, a difference of 11 keV from the weighted average of Penning-trap measurements.

^{106}Sn: The mass excess of ^{106}Sn published in AME 2020 is presented as a weighted average of two Penning-trap measurements performed at JYFLTRAP [62] and SHIPTRAP [63] with a value of −77354(5) keV. The result of this analysis gives a mass excess of −77327(37) keV, a difference of 26 keV from the weighted Penning-trap measurements.

^{107}Sn: The mass excess of ^{107}Sn published in AME 2020 is that of a Penning-trap measurement performed at JYFLTRAP with a value of −78512(5) keV [62]. The mass excess determined by this work is −78511(34) keV, a 1 keV difference from the Penning-trap determination, showing excellent agreement.

3.6 Discussion

3.6.1 Two-Neutron Separation Energy

From the mass values determined, the two-neutron separation energy (the energy required to remove two neutrons from the nucleus) S_{2n} was calculated for $^{104-107}$Sn from:

$$S_{2n}(N,Z) = m(Z,N-2) - m(Z,N) + 2m_n \tag{3.13}$$

where m_n is the mass of a neutron. The uncertainty of the TITAN S_{2n} values are calculated as

$$\delta S_{2n}(N,Z) = \sigma_{S2N,\ m_A} = \sqrt{\sigma^2_{m_A} + \sigma^2_{m_{A-2}} + \sigma^2_{m_n}} \tag{3.14}$$

where $\sigma_{m_n} = 4.73 \times 10^{-10}$ keV [60]. For example, the error of the two-neutron separation energy of ^{107}Sn is

$$\sigma_{S2N,\ m_{107}} = \sqrt{\sigma^2_{m_{107}} + \sigma^2_{m_{105}} + \sigma^2_{m_n}} \ . \tag{3.15}$$

In Figure 3.8, we update the S_{2n} found in AME 2020 by averaging them with this work.

Exploring two-neutron separation energy gives insight into the structure of nuclei. Referring back to Figure 1.2, S_{2n} usually monotonically decreases with increasing N. The slope is nearly linear with kinks at so-called magic numbers (e.g. $N = 50$ in Figure 1.2). Deviations from this near universal behaviour can indicate deformation, new shells (i.e. an unexpected kink in S_{2n}), unbound nuclei, or other, more complicated behaviour. In Figure 3.8, we see the general linearly decreasing S_{2n} with increasing N, indicative of mid-shell behaviour. Furthermore, no deviation from linearity (e.g. a sign of deformation) was observed in this work. The TITAN results align well with the evaluated data from AME 2020 [60], reinforcing the evidence for the existence of the $N = 50$ shell closure as dictated by the nuclear shell model [66].

The uncertainties achieved in this TITAN MR-TOF MS experiment, in a mere four hours of measurement time, were sufficient to probe nuclear shells and the evolution of nuclear structure towards the neutron dripline. Unfortunately, due to a site-wide power failure, the experiment was halted before more nuclides towards $N = Z = 50$ could be measured; however, due to the highly sensitive nature of the TITAN MR-TOF MS, further measurements towards the dripline are within reach. The lowest rates detected in this experiment were 0.02 particles per second (pps) (for ^{104}Sn) however, rates as low as 0.0007 pps have been detected and measured [50] at TITAN. Therefore, the low rates of tin as we approach the dripline are well within the sensitivity-range of the TITAN MR-TOF MS.

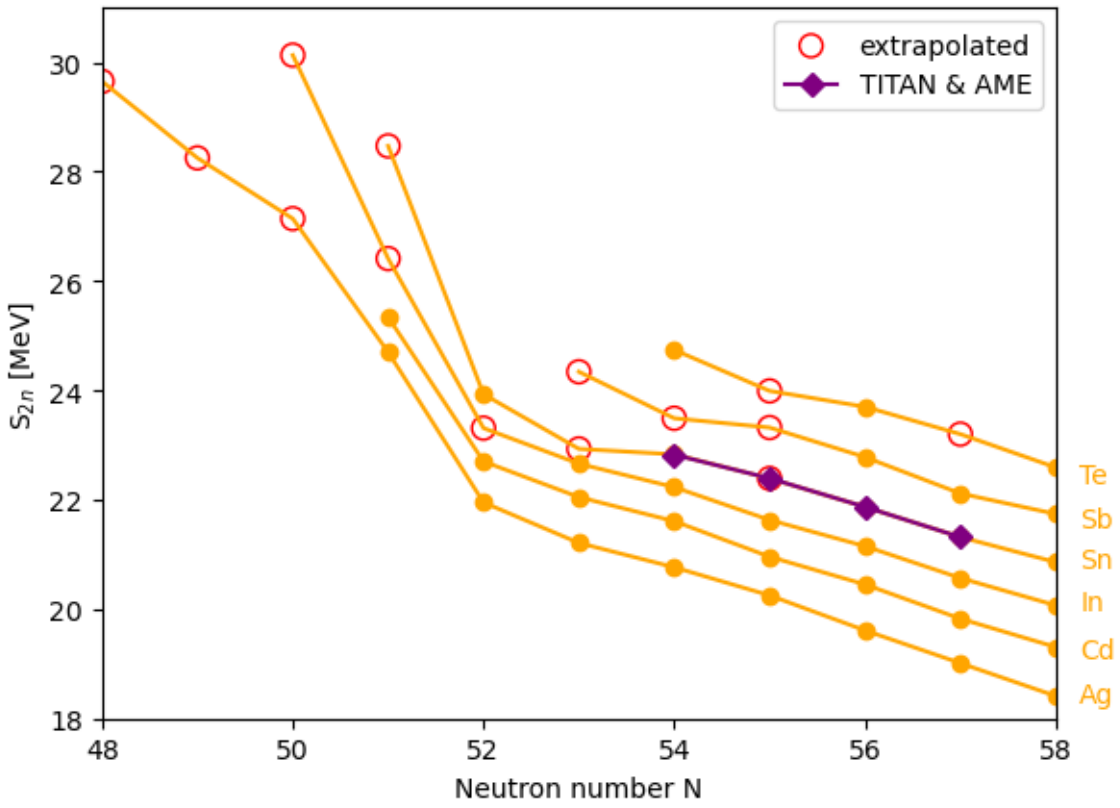

Figure 3.8: Two-neutron separation energy S_{2n} in the region of $N = 48 - 58$. The TITAN values have been combined with literature results using a variance-weighted mean and are depicted in purple. Red circles indicate extrapolated values by the authors of AME 2020, as opposed to solid orange circles which represent empirically derived values. Due to the MeV scale of S_{2n}, the δS_{2n} are too small to see. S_{2n} usually decreases linearly following a steep drop ($N = 50$ in this figure), with the rapid decrease indicating a shell closure. Furthermore, any places with deviation from linearity indicate more complicated structure of nuclei e.g. deformation. The TITAN values support typical linear-like, mid-shell behaviour, supporting the neutron-shell closure at $N = 50$.

3.6.2 First Measurements of ^{89}Zr and ^{90,91}Y

Due to the broadband nature of the MR-TOF MS technique, we were able to perform the first direct mass measurements of ^{89}Zr and ^{90,91}Y, with all three results in agreement with AME 2020. The simultaneous measurement of the tins with ^{89}Zr and ^{90,91}Y may be surprising; however, the Zr and Y formed oxide molecules and, ergo, were isobars of the tins. This work showcases how the innate contamination involved in RIB production may lead to additional measurements outside the initial scope of interest. The first direct mass measurements of these nuclides serve as critical anchoring points for long chains of indirect

and/or extrapolated mass surfaces. Direct mass measurements are preferred over indirect methods, such as β-endpoint energy measurements, since they are both accurate and precise, whereas indirect methods are prone to the propagation of errors.

For example, ^{90}Br is five β^- decays away from stability. Measurements of endpoint energies ($Q_{\beta-}$) from ^{90}Br to ^{90}Y were performed [67], with the $Q_{\beta-}$-value of ^{90}Y being determined through (n,γ) and (d,p) measurements of stable ^{89}Y (see [60] and references therein). So, as of 1981, the measured mass of ^{90}Br depended on the mass determination of four other short-lived species. Finally, in 2006 and 2007, the mass of ^{90}Br and its daughter were directly measured [68, 69] and the determined $Q_{\beta-}$-value deviated from the 1981 value by 1.2 MeV (or 2.9σ)! The discrepancy in the β-endpoint energy measured for ^{90}Br underscores the need for accuracy *and* precision, typically best achieved by direct techniques. Therefore, the direct measurements of ^{89}Zr and ^{90,91}Y presented in this work provide essential reference points to anchor similar chains of indirect measurements.

In conclusion, the TITAN measurements performed are in excellent agreement with the values reported in the literature, with differences of less than 1σ in the tin cases. The precision achieved in this campaign enabled the exploration of nuclear shells, with the tin S_{2n} inquiry showing indicative, mid-shell behaviour, in agreement with literature and what is expected from the nuclear shell model. Furthermore, the first direct measurements of ^{89}Zr and ^{90,91}Y serve as critical reference points for sequences of indirect measurements. These results underscore the importance of direct measurements and highlight the multifaceted capability of the MR-TOF MS method for exploring regions of both stability and towards the nuclear driplines.

Chapter 4

Measurement Penning Trap

4.1 Overview

Penning traps confine ions in three dimensions by means of a strong magnetic field and a weak electrostatic field. The electric field traps ions in the axial direction (here parallel to the $\vec{B}$ field) whereas the magnetic field traps ions in the radial direction. Determining the mass m of an ion of charge q inside a Penning trap requires the precise measurement of the cyclotron frequency,

$$\nu_c = \frac{qB}{2\pi m} \quad . \tag{4.1}$$

The following sections detail ion confinement, motion, and manipulation in a Penning trap and the mass measurement techniques.

4.2 Ion Confinement

Recall from Chapter 2.5, axial confinement of ions is realized by applying an electric field of the form

$$V(r,z) = \frac{V_0}{4d_0^2}(2z^2 - r^2) \tag{4.2}$$

on the hyperbolic electrodes, where V_0 is the trapping voltage and $d_0 = \sqrt{z_0^2/2 + r_0^2/4}$ is the characteristic dimension of the trap with z_0 and r_0 are the axial and radial coordinates with respect to the z-axis (can be seen in Figure 2.6). This potential is realized by two end cap electrodes, a ring electrode, and two sets of correction electrodes (called guards and tubes). Radial confinement for MPET is accomplished by a strong magnetic field provided by a 3.7 T superconducting solenoid magnet.

4.3 Ion Eigenmotions

Due to the magnetic and electric fields, ions move with three characteristic motions when in a Penning trap: axial motion (ν_z), reduced cyclotron motion (ν_+), and magnetron motion (ν_-). For a full derivation of ion motion in a Penning trap, please refer to [70]. The eigenfrequencies are

$$\nu_+ = \frac{\nu_c}{2} + \sqrt{\frac{\nu_c^2}{4} - \frac{\nu_z^2}{2}} \quad \text{reduced cyclotron motion} \tag{4.3}$$

$$\nu_- = \frac{\nu_c}{2} - \sqrt{\frac{\nu_c^2}{4} - \frac{\nu_z^2}{2}} \quad \text{magnetron motion} \tag{4.4}$$

$$\nu_z = \frac{1}{2\pi}\sqrt{\frac{qU}{md^2}} \quad \text{axial motion,} \tag{4.5}$$

and the hierarchy of these motions is

$$\nu_c > \nu_+ \gg \nu_z \gg \nu_-. \tag{4.6}$$

where

$$\nu_c^2 = \nu_+^2 + \nu_-^2 + \nu_z^2. \tag{4.7}$$

Since $\nu_c \gg \nu_-$ and $\nu_+ \gg \nu_-$, the following approximation can be used [70]:

$$\nu_c = \nu_+ + \nu_-. \tag{4.8}$$

At TITAN, these frequencies are on the order of $\nu_c \approx 1.458$ MHz, $\nu_+ \approx 1.452$ MHz, $\nu_z \approx 133500$ Hz, and $\nu_- \approx 6100$ Hz (for $^{39}K^+$).

4.4 Ion Manipulation

Central to PTMS is the manipulation of the eigenmotions of an ion. In doing so, we can change how energy is distributed between the different eigenmotions. Taking $\omega = 2\pi\nu$, the energy of each motion is [70]

$$E_z = \frac{m}{2} r_z^2 \omega_z^2 \tag{4.9}$$

$$E_+ = \frac{m}{2} r_+^2 \left(\omega_+^2 - \omega_+\omega_-\right) \tag{4.10}$$

$$E_- = \frac{m}{2} r_-^2 \left(\omega_-^2 - \omega_+\omega_-\right) \tag{4.11}$$

with r_- and r_+ corresponding to the radii of the respective eigenmotions and r_z is the axial trajectory (z direction). When the radius of the orbit is altered, so is the energy of its motion. At TITAN, this is done by applying radio frequency (RF) fields [31] to the segmented ring electrode, seen in Panel A of Figure 4.1. This process is called excitation,

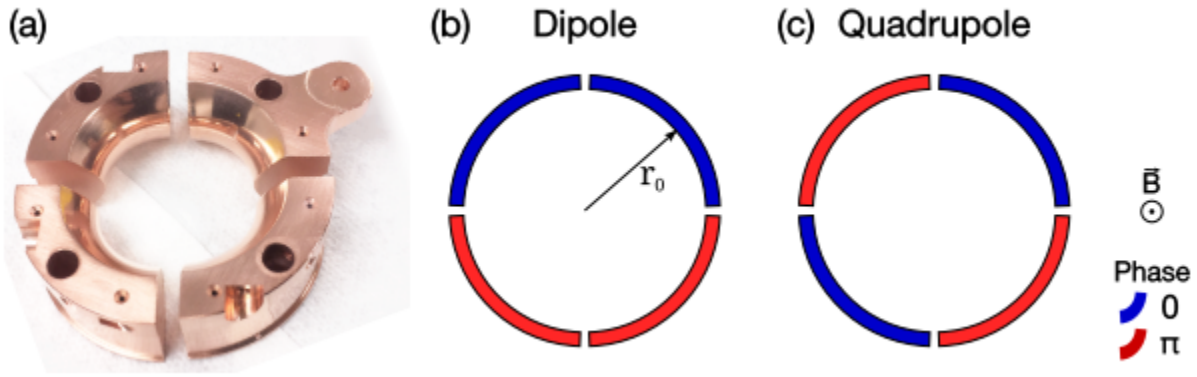

Figure 4.1: Panel A: Disassembled segmented ring electrode. Panel B: Electrode configuration for dipole excitation. Panel C: Electrode configuration for quadrupole excitation.

and two types of radial excitations are typically used at TITAN: dipole and quadrupole. In a dipole excitation, each half of the ring is π out of phase from one another, seen in Panel B of Figure 4.1. For a quadrupolar excitation, the RF phase applied to each electrode is offset π nearest neighbours, seen in Panel C of Figure 4.1. The applied RF is of the form [31]

$$U_{RF}(t) = U_{RF,0}\cos(\omega_{RF}t + \phi_{RF}) \tag{4.12}$$

with $U_{RF,0}$ being the amplitude of the RF, ω_{RF} being the frequency of the RF, and ϕ_{RF} being the phase of the RF. For the techniques used in RIB PTMS, the focus is on the radial eigenmotions.

4.4.1 Dipole Excitations

With a dipole excitation, a dipole field of the form [31]

$$\frac{U_{RF}}{U_{RF,0}} = \frac{y}{r_0}\cos(\omega_{RF}t + \phi_{RF}) \tag{4.13}$$

is created, with r_0 being the distance from the trap center to the ring electrode, as highlighted in Panel B in Figure 4.1. When the frequency of the RF applied ν_{RF} is that of ν_- or ν_+, its corresponding eigenmotion is excited. This is useful to prepare ions to a particular orbit by

exciting a specific frequency. For example, this is valuable in phase imaging, where an ion needs to be excited to an initial radius for the measurement procedure to commence.

4.4.2 Quadrupole Excitations

With quadrupole excitation, a field of the form [31]

$$\frac{U_{RF}}{U_{RF,0}} = \frac{2xy}{r_0^2}\cos(\omega_{RF}t + \phi_{RF}) \tag{4.14}$$

is created. This excitation (when $\omega_{RF} = \omega_- + \omega_+ = \omega_C$) couples the radial eigenmotions and in doing so, causes a beating between reduced cyclotron and magnetron. The conversion from magnetron to reduced cyclotron motion increases the radial kinetic energy of ions (described further in Section 4.5) and, thus, decreases their TOF to the detector. Quadrupolar excitations are essential to measurements with PTMS that are discussed below.

4.5 Time-of-Flight Ion-Cyclotron-Resonance Technique for Mass Measurements

The Time-of-Flight Ion-Cyclotron-Resonance (TOF-ICR) technique [31] is a method of mass spectrometry which relies on measuring an ion's time of flight from the trap to the detector. As the ions travel away from the trapping region, the gradient of the magnetic field induces a force

$$\vec{F} = \vec{\nabla}(\vec{\mu}\cdot\vec{B}) \tag{4.15}$$

where μ is the magnetic dipole moment of the ion, defined as

$$\vec{\mu} = -\frac{E_{\text{r, kin}}}{B}\hat{z} \tag{4.16}$$

where $E_{\text{r, kin}}$ is the ion's radial kinetic energy. Resonant ions (i.e. ions excited at their cyclotron frequency) will experience a greater (axial) force, since the kinetic energy is proportional to the excitation frequency, and therefore, will have the shortest TOF.

TOF-ICR begins with ions having a well-defined radius $\rho_- \neq 0$ and $\rho_+ = \rho_z = 0$ in the trap. At TITAN this is can be accomplished with so-called Lorentz steerers [71]: These electrostatic elements in the beamline use $\vec{E}\times\vec{B}$ drift to drive ions to a defined radius, ρ_-, or via a dipole excitation to excite ions to a specifc radius. Then, a quadrupole excitation is applied at ν_{RF} at frequencies near and at ν_c for a time t_{RF}. Recall that when a range of frequencies around ν_c are used during excitation, one can partially convert ion motion between the two radial eigenfrequencies. When the applied frequency is equal to the cyclotron

frequency i.e. $\nu_{RF} = \nu_c$, motion is fully converted between magnetron motion and reduced cyclotron motion. After the quadrupole pulse is applied, ions are ejected and sent towards an MCP which measures the flight time of ions. The time of flight of ions is given by [31]

$$TOF = \int_0^{z_d} \sqrt{\frac{m}{2\left[E_0 - qU(z) + |\mu(E_r)B(z)|\right]}}\, dz \tag{4.17}$$

where 0 is the position of the trap center, z_d is the position of the detector, E_0 is the initial kinetic energy of the ion, q is the charge of the ion, $U(z)$ is the electric potential the ion passes through, μ is the magnetic dipole moment of the ion, and $B(z)$ is the magnetic field strength. This is a minimum when there is a full conversion between motions as kinetic energy is increased through conversion, resulting in the global minimum of a time of flight when $\nu_{RF} = \nu_c$, as seen in Figure 4.2. An analytic fit of Equation 4.17 to the data determines ν_c at the minimum.

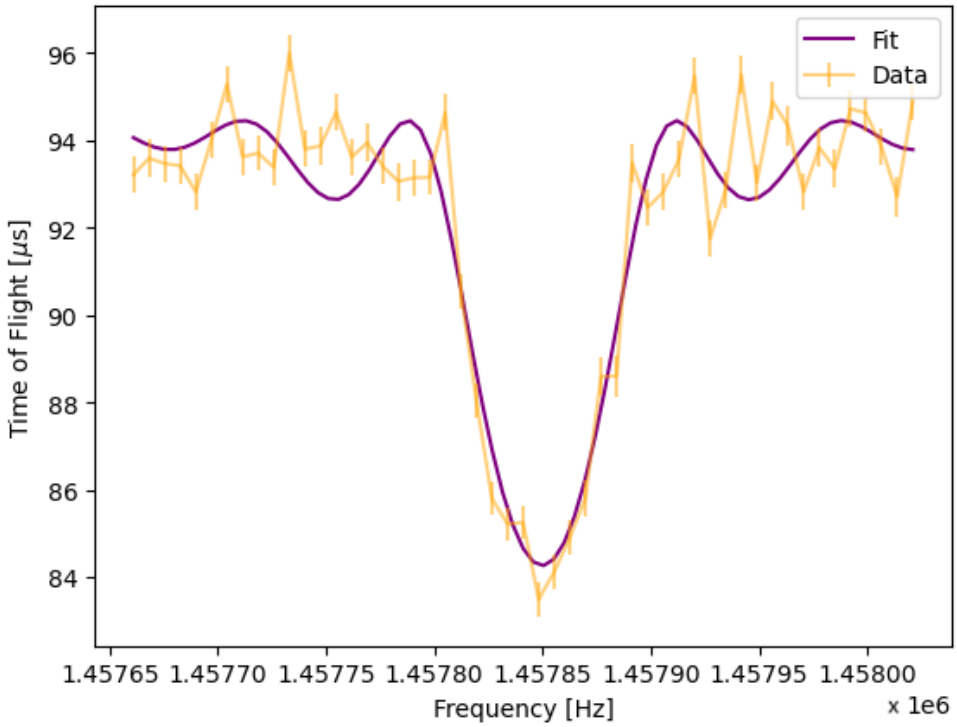

Figure 4.2: Example of TOF resonance of $^{39}K^+$ with an excitation time of 14 ms (shown in orange). The frequency corresponding to the global time-of-flight minimum is the cyclotron frequency which is used to determine the mass. The purple curve is a fit using Equation 4.17 [31].

To account for magnetic field fluctuation and since B is typically best determined using

the cyclotron frequency of a well-known mass ($\nu_{c,\text{ ref}}$), a ratio between frequencies (R_ν), is determined:

$$R_\nu = \frac{\nu_{c,\text{ ref}}}{\nu_c} = \frac{m_a - qm_e}{m_{a,\text{ref}} - q_{\text{ref}}m_e}\frac{q_{\text{ref}}}{q} \tag{4.18}$$

where m_a is the atomic mass of the ion of interest, q is the charge of the ion of interest, m_e is the mass of an electron, $m_{a,\text{ref}}$ is the atomic mass of the reference ion, and q_{ref} is the charge of the reference ion.

Since the implementation of the Penning trap at TITAN in 2007, the TOF-ICR method has been used to measure more than 86 nuclei [22]. With typical precision at a level of one part per billion ($\delta m/m \sim 10^{-9}$) [22], studies of the weak interaction and physics beyond the Standard Model were done.

Due to the fact that it is a scanning technique, no prior knowledge of the ion is required, unlike the PI-ICR technique described in the next section. The precision of this method is [72]

$$\frac{\delta m}{m} \propto \frac{m}{qBT_{RF}\sqrt{N}} \tag{4.19}$$

where T_{RF} is the time duration of the RF excitation and N are the number of detected ions. Since the precision is proportional to $1/q$, the use of highly charged ions – which TITAN is uniquely set up for – can boost precision. This technique is not without its disadvantages: The resolving power, given by [72]

$$R \propto \frac{qBT_{RF}}{m} \tag{4.20}$$

is limited by the duration of the excitation, which, consequently, is limited by the nuclide's halflife. Furthermore, tens of ions are needed to create a resonance, whereas the next technique discussed needs only two in principle.

4.6 Phase-Imaging Ion Cyclotron Resonance Technique for Mass Measurements

The Phase-Imaging Ion-Cyclotron-Resonance (PI-ICR) technique [32] is a newer method that determines the cyclotron frequency of an ion by measuring the phase evolution of ion motion after excitation-free motion within the trap as projected onto a position-sensitive detector. The principle of PI-ICR is shown in Figure 4.3.

Generally, an ion in the presence of a magnetic field will orbit with angular frequency ω. For a time t, the total phase traversed, ϕ_{total}, relates to the frequency via

$$\nu = \frac{\phi_{\text{total}}}{2\pi t} = \frac{\phi + 2\pi N(t)}{2\pi t} \tag{4.21}$$

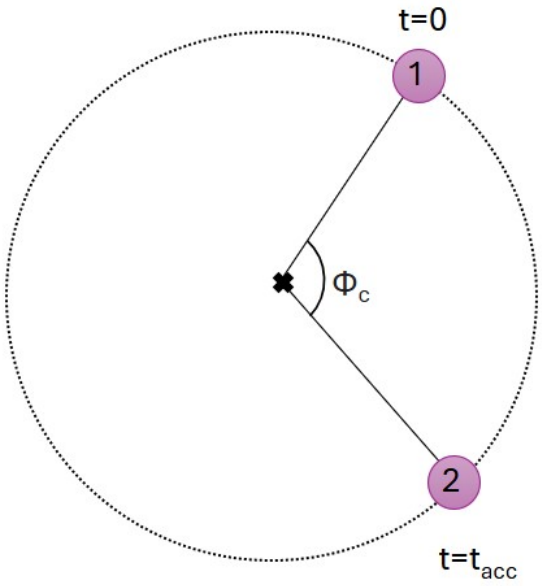

Figure 4.3: Measurement principle of the PI-ICR technique. Position 1 indicates the so-called reference and position 2 indicates the final spot. The angle between them ϕ_c is used to determine the cyclotron frequency. Figure inspired by [32].

where $\nu = \omega/2\pi$, ϕ is the excess phase (i.e. $\phi = \phi_{\text{total}} - N(t) \times 2\pi$), and $N(t)$ are the number of revolutions the ion completes in time t. Therefore, to determine the frequency, we must first determine the center of the orbit and the initial and final locations of the ion to establish ϕ and $N(t)$. This general concept translates directly to PI-ICR where the determination of the center of the orbit and the initial and final positions of the ions is necessary to determine the phase and number of revolutions.

There are two ways to measure the cyclotron frequency [73]: independent or simultaneous measurements of the radial motions corresponding to ν_+ and ν_- (and employing $\nu_c = \nu_+ + \nu_-$). Since the simultaneous method provides a more direct and efficient determination of the cyclotron frequency, it is the method of choice in this work. In this routine, two measurement schemes are needed: so-called "reference" and "final". The reference and final schemes only differ in the timing of when the quadrupole excitation is applied, as discussed below.

First, ions are injected into the center of the trap. At TITAN, this is done using a Lorentz steerer [71] to minimize any initial ion motion. Then, a dipole excitation at $\nu_{RF} = \nu_+$ excites ions to a well-defined radius. In the reference scheme, immediately after the dipole excitation, a quadrupole excitation is applied, converting the ion's eigenmotion from the high-frequency reduced-cyclotron motion to the lower-frequency magnetron motion. After accumulating

phase during time $t_{\text{acc}} = t_{\text{total}}$, ions are ejected towards a positive-sensitive multi-channel plate (MCP) detector, and as the ion traverses through radially symmetric optics to the MCP, its relative phase is preserved. In the final scheme, ions revolve and accumulate a phase during an accumulation time $t_{\text{acc}} = t_1$ after the dipole excitation at $\nu_{RF} = \nu_+$. Then, a quadrupole excitation at $\nu_{RF} = \nu_c$ is applied. After additional revolution in the trap for a time duration of t_2, ions are ejected. The total phase accumulation time of the ion in the trap is defined as $t_{\text{total}} = t_1 + t_2$, and when t_{total} is constant for both schemes, the phase between the two spots can be described by [73]

$$\phi_c = \phi_{\text{final}} - \phi_{\text{reference}} = 2\pi[N(t_{\text{acc}}) - \nu_c t_{\text{acc}}], \tag{4.22}$$

which can be rearranged to get

$$\nu_c = \frac{\phi_c + 2\pi N(t_{\text{acc}})}{2\pi t_{\text{acc}}} \quad . \tag{4.23}$$

Since this technique relies on precise position measurements, the MPET detector was upgraded. The position-sensitive detector, a Roentdek DLD40 [74], reconstructs positional information via two perpendicular delay lines. When ions strike the front of the MCP, they generate secondary electrons, which are driven towards the back of the MCP onto the delay line by an applied positive potential. These electrons then drift towards the delay lines, and when they strike the line, they create an electrical signal that is sent along the lines. The signals are then input into a time-to-digital converter and the time difference between the signals reaching the ends of the wire is measured. From this timing difference, the position of impact can be precisely reconstructed.

PI-ICR is in the process of being implemented at TITAN and, once complete, can offer a five-fold gain in precision as compared to the TOF-ICR method, reaching a level of $\delta m/m \sim 10^{-10}$ [32]. Through simulations, the resolving power of PI-ICR has shown to scale with the charge state: $R \propto Q^{2.5}$ [75]. Therefore, resolving power and precision can be increased by using highly charged ions, which TITAN is uniquely equipped for with the EBIT (recall, the EBIT can create highly charged ions that can then be transported to MPET). The precision of this technique is given by [73]

$$\frac{\delta m}{m} = \frac{\Delta r}{\nu_c \pi r t_{acc} \sqrt{N}} \tag{4.24}$$

where Δr is the radial spread of clusters and r is the radius with respect to the center of the orbit. An additional benefit of this technique is that, in principle, only two ions are

needed to perform a measurement. However, since this technique depends on preserving the radial phase, maintaining a radially symmetric path from the trap to the detector is essential. In practice, however, achieving this precise symmetry is challenging. Furthermore, the detector must be precisely aligned as not to introduce an "ellipticity of the orbit image" [73]. Moreover, this method requires some prior knowledge of the ion in order to determine its mass; therefore, is not ideal for nuclide and isomer discovery (unlike the TOF-ICR method).

Chapter 5

Developments Towards Phase-Imaging Implementation at TITAN

For on-line analysis of Phase-Imaging Ion-Cyclotron Resonance (PI-ICR) data at TITAN, a previously created analysis suite was updated for this thesis. The following sections describe how the Phase-Imaging Analysis Tool (PhIAT) operates, the upgrades completed as part of this work, and the first tests of PhIAT. Furthermore, the timing scheme for PI-ICR measurements was added to the data acquisition system (DAQ).

5.1 Phase-Imaging Analysis Tool

The Phase-Imaging Analysis Tool (PhIAT) processes raw data generated by the Measurement Penning Trap (MPET) data acquisition system to output the cyclotron frequencies and masses of the ion(s) of interest. PhIAT is implemented in MATLAB and Python and features a graphical user interface (GUI). The complete code is available at [76]. For testing purposes, data was simulated using the Tool for Ion Phase Simulation (TIPS), as detailed in Appendix A.1.

In the fitting procedure, detected ion "spots" are clustered using the mean shift algorithm [77]. Then, the x and y centroids of the clusters are determined by fitting 2D Gaussian distributions to the clusters using a maximum likelihood estimator (see Equation 3.5), with the mean and standard deviation of the distributions corresponding to the center of the detected ions and to its error, respectively. An example of this process can be seen in Figure 5.1. Next, the phase ϕ_c is determined via

$$\phi_c = \arccos\left(\frac{b^2 + c^2 - a^2}{2bc}\right), \; 0 \leq \phi \leq 180^\circ \tag{5.1}$$

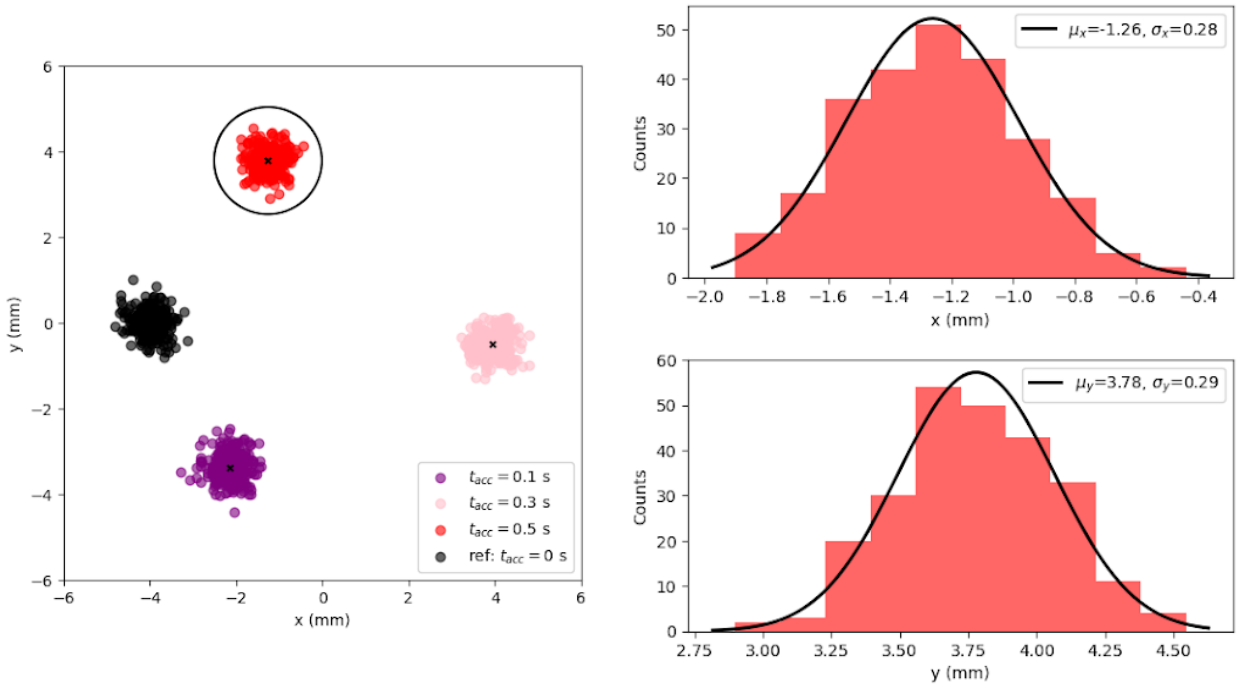

Figure 5.1: Example of PhIAT fitting procedure with data simulated using TIPS. The histograms on the right are of the circled cluster on the left. The black 'x' at the center of the coloured clusters represents the center of the cluster ($\mu_{x,y}$ labeled on the two right hand side plots) determined by fitting a 2D Gaussian distribution to the data. Inspired by [78].

$$\phi_c = 180^\circ - \arccos\left(\frac{b^2 + c^2 - a^2}{2bc}\right), \ 180^\circ < \phi < 360^\circ \tag{5.2}$$

where a, b, and c are defined in Figure 5.2 and angles in PhIAT are defined in Figure 5.3. In terms of the trap center (x_{cen}, y_{cen}) and centers of the final (x_{fin}, y_{fin}) and reference spots (x_{ref}, y_{ref}), these parameters can be expressed as

$$a = \sqrt{(x_{\text{ref}} - x_{\text{fin}})^2 + (y_{\text{ref}} - y_{\text{fin}})^2} \tag{5.3}$$

$$b = \sqrt{(x_{\text{ref}} - x_{\text{cen}})^2 + (y_{\text{ref}} - y_{\text{cen}})^2} \tag{5.4}$$

$$c = \sqrt{(x_{\text{fin}} - x_{\text{cen}})^2 + (y_{\text{fin}} - y_{\text{cen}})^2} \tag{5.5}$$

With the angle determined, PhIAT next calculates the number of revolutions that the ion made in the trap during the accumulation time, $N(t_{\text{acc}})$. An initial estimate is made by taking

$$N(t_{\text{acc}}) \approx \omega_c^0 t_{\text{acc}} \tag{5.6}$$

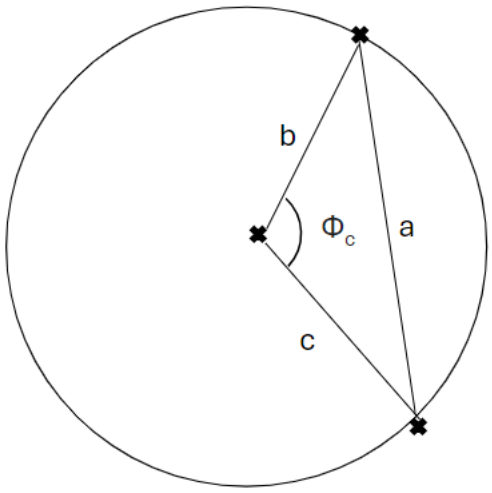

Figure 5.2: Definition of distances a, b, and c with respect to the center of orbit for determination of the angle ϕ_c. Adapted from [32].

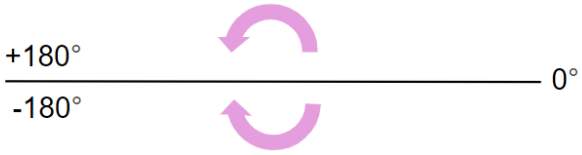

Figure 5.3: Angle definitions within PhIAT. Spots in the south will be defined with negative angles, from 0 to $-180°$ and spots in the north will be defined with positive angles, from 0 to 180°.

where ω_c^0 is calculated from AME [60]. From this initial estimate, a range of $N(t_{\text{acc}})$ values are created $N(t_{\text{acc}}) = N(t_{\text{acc}}) \pm N_{\text{range}}$. Each value of $N(t_{\text{acc}})$ is then input in Equation 4.23 to create a list of cyclotron frequencies. To determine the true cyclotron frequency, PhIAT compares two or more files with different accumulation times. After determining the cyclotron frequency, the mass is determined via

$$m = \frac{q}{q_{\text{cal}}} \frac{\omega_{c,\text{cal}}}{\omega_c} (m_{\text{cal}} + Q_{\text{cal}} m_e) + Q m_e \tag{5.7}$$

where $\omega_{c,\text{cal}}$ is the cyclotron frequency of the well-known calibrant ion to determine the

magnetic field (see Equation 4.18), Q_{cal} is its charge state, and m_{cal} is its mass.

5.2 Upgrades to PI-ICR Analysis Tool (For this Thesis)

5.2.1 Uncertainty in Angle Determination

To determine the uncertainty in the angle between spots, the following has been added to PhIAT for testing and troubleshooting purposes. The angle ϕ between spots is calculated via

$$\phi = \arctan\left(\frac{y - y_{\text{cen}}}{x - x_{\text{cen}}}\right) \quad . \tag{5.8}$$

Error propagation yields the following

$$\delta\phi = \sqrt{\left(\frac{y_{\text{cen}} - y}{(x - x_{\text{cen}})^2 + (y - y_{\text{cen}})^2}\delta x\right)^2 + \left(\frac{x + x_{\text{cen}}}{(x - x_{\text{cen}})^2 + (y - y_{\text{cen}})^2}\delta y\right)^2}, \tag{5.9}$$

where the error in the x_{cen} and y_{cen} have been omitted (as this was added for visualization and testing purposes). The result of $\delta\phi$ is then converted from radians to degrees by multiplying the output of Equation 5.9 by $180°/\pi$. The output is given when the user selects "Automatic Fit" with "Create Freq. ID" checked, and is found in the frequency ID output file.

5.2.2 First Test: Fitting Ideal and Non-Ideal Clusters

Recall, the PI-ICR technique relies on the preservation of phase between the trap and the detector. The difficulty of this lies in, for example, the alignment of the trap with the detector and the magnetic field. As fully described in [73], another possible contribution to the distortion of cluster shape is deviation from an ideal harmonic trapping potential. Furthermore, it is expected that before fine tuning of the system, the detected ion clusters will not be ideal, 2D Gaussian distributions. Therefore, it is of utmost importance that PhIAT is able to perform, under both ideal and non-ideal conditions.

To demonstrate PhIAT's functionality at fitting ideal and skewed spots, data was simulated using TIPS and analyzed with PhIAT. Three accumulation times (t_{acc}) were considered, with all simulation settings listed in Appendix A.1.1. Figure 5.4 shows simulated clusters. The accumulation times used in the simulation were chosen to illustrate the evolution of phase while still being typical PI-ICR accumulation times. The PhIAT fitting parameters were kept the same for both analyzes with 20 ions per cluster and a 1.25 mm spot bandwidth.

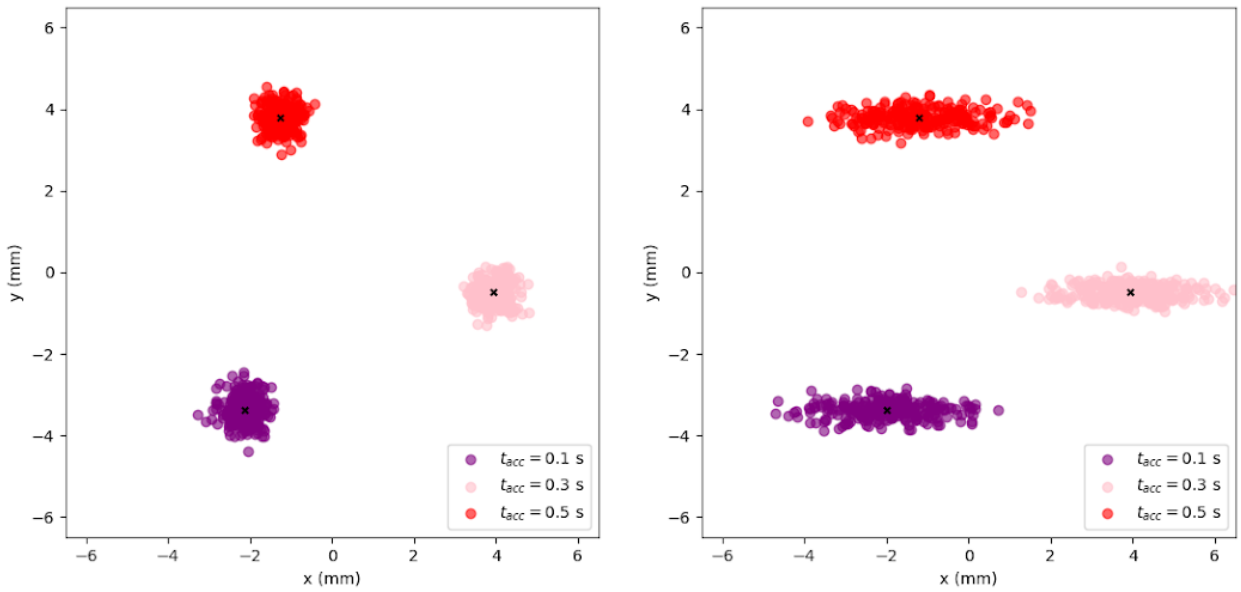

Figure 5.4: Simulated ideal (left) and skewed (right) clusters for $\nu_c =$ Hz. The horizontal and vertical axes represent the x and y detector axes, respectively, and are in units of millimeters (mm). Simulation settings are available in Appendix A.1.1.

From the PhIAT analysis, the determined cyclotron frequency agrees within error to the input cyclotron frequency for both ideal and skewed clusters. As demonstrated by the success of the PhIAT in the analysis of both ideal and skewed clusters, it has shown its capability as a tool for beam diagnostics and analysis of phase-based data as part of the implementation of PI-ICR at TITAN.

5.2.3 Probing Systematic Error Related to Non-Ideal Injection

PhIAT was initially created for the Canadian Penning Trap (CPT), where the cyclotron frequency appeared to vary sinusoidally in time [79]. This process occurs when an ion has non-zero initial magnetron motion, likely due to non-ideal injection. Then, when a dipole excitation is applied to excite the ion to an initial radius, because it has some initial motion, it does not precess about the center with pure reduced cyclotron motion. Instead, the motion will be a combination of reduced cyclotron motion and magnetron motion which eventually results in the cyclotron motion appearing to vary sinusoidally. Full details on these effects can be found in [79]. To account for this, PhIAT automatically fit a three-parameter sinusoidal curve to cyclotron frequencies at different accumulation times. At TITAN, injection into the

trap has been optimized using a Lorentz steerer [71] which can minimize initial ion motion, which may reduce the likelihood of this sinusoidal behaviour. In order to preserve the PhIAT program and its multitude of capabilities, the sine curve fitting procedure is now optional and only proceeds if the user selects the "Sine Curve Fitting?" option in the PhIAT GUI.

5.2.4 Streamlined Program Initialization

Previously, PhIAT was hosted on a personal GitHub account. In order for PhIAT to be maintained long-term by the greater TITAN Collaboration, it is now hosted on a TITAN-based GitHub, available at [76]. Furthermore, a documentation site was created as part of this work which can be located at [80].

Finally, the process for importing data files was upgraded by replacing manual entry with a directory tree visualization. Within this, the loading process was streamlined to import only user-selected files. Previously, entering a directory path to a folder would load all files within it, which could be problematic since not all files are relevant to the same analysis and it was not possible to make selections (since only a directory was entered). This adjustment now ensures that only specified files are loaded. Additionally, single-file loading was enabled which facilitates live troubleshooting, tuning, and debugging. Furthermore, within the new loading procedure, PhIAT's programming needed to distinguish between simulated and real data, as real data is imported as raw files requiring conversion to a PhIAT-compatible format, whereas simulated data is already prepared in this format. PhIAT is now able to make this distinction within the new procedure. Lastly, file exporting was updated. The export function now automatically creates a new directory, including a copy of the data for quick analysis comparisons and to safeguard against input file corruption. This directory is timestamped with the current date and time, and results are saved to a user-defined location. These procedures were rigorously tested with data output from the MPET DAQ and simulated data created with TIPS to ensure compatibility with both formats.

5.3 Implementation of PI-ICR Timing Scheme (For this Thesis)

The MPET DAQ is run under the Maximum Integrated Data Acquisition System (MIDAS) structure [81] which is connected to the Experimental Physics and Industrial Control System (EPICS) [82]. MIDAS and EPICS work with an arbitrary function generator to apply and split the RF signal to the segments of the ring electrode, with the timing dictated by the programmable pulse generator (PPG).

To support the implementation of PI-ICR at TITAN, the PPG section of the MPET

DAQ was updated as part of this work. As a result, the MPET DAQ has two modes of measurement: TOF-ICR and PI-ICR, with their respective schemes displayed in Figure 5.5.

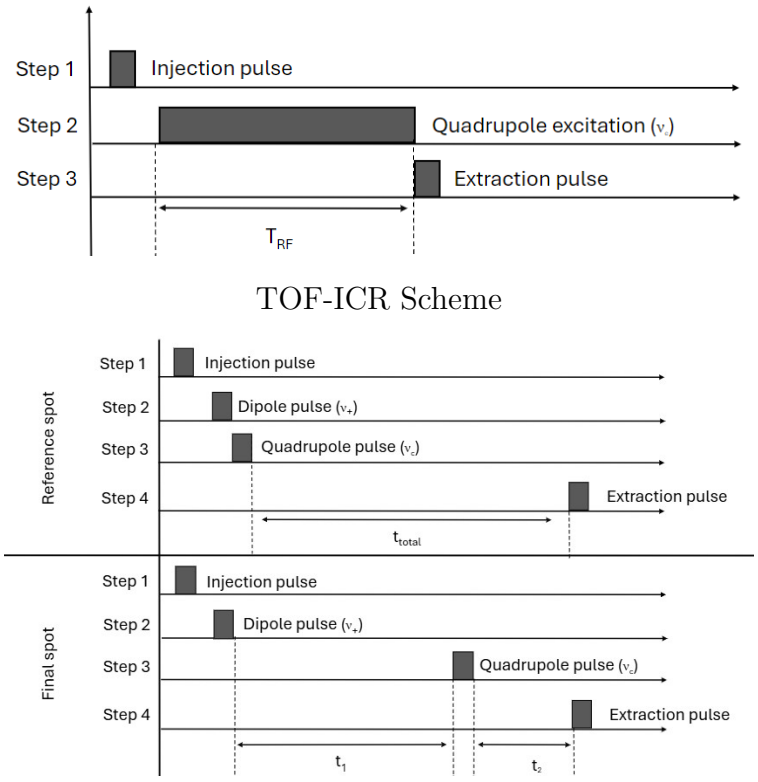

Figure 5.5: Timing schemes of the measurement techniques in use at TITAN MPET. Both figures have arbitrary pulse sizes and lengths; additionally, some steps have been omitted for illustrative clarity. Top: pulse scheme of the TOF-ICR technique. Bottom: pulse scheme of the PI-ICR technique. Figure inspired by [32, 78, 83].

The ensure the relation $t_{\text{total}} = t_1 + t_2$ is held constant between reference and final measurements, the PPG has been programmed with the following variable adjustment: $t_{\text{total}} = T$, $t_1 = t_{\text{acc}}$, and $t_2 = T - t_{\text{acc}}$. By inspection, when $t_{\text{acc}} = 0$, we are preforming a reference spot measurement. This variable rearrangement allows $t_{\text{total}} = T$ to be held constant and allows the user to only change the accumulation time, t_{acc}, which mitigates user-error. The limitation lies in the fact that $T > t_{\text{acc}}$. To account of this, the DAQ has been programmed to output an error message if the user-entered t_{acc} is greater than T.

Switching between TOF-ICR and PI-ICR measurement schemes is easily accomplished through the MPET DAQ's "Save and Load" functionality, where the PI-ICR scheme has been

saved to and is readily accessible. Additionally, the visualizer at the bottom of the DAQ PPG screen is now exportable. This improvement offers a useful visual tool, such as for comparing schemes with varying accumulation times. The next step to ensure functionality is to test the new timing scheme with an off-line source. In summary, the implementation of the timing scheme for PI-ICR in the MPET DAQ is a crucial step forward in advancing the integration of PI-ICR with TITAN.

In summary, PhIAT enables the analysis of on-line, phase-based data as part of the ongoing implementation of PI-ICR at the TITAN facility. Through an interactive GUI, it provides a user-friendly interface for both tuning and conducting PI-ICR measurements. In this work, uncertainty in angle determination has been incorporated, and the successful clustering and fitting of simulated data with PhIAT has been demonstrated. The results highlight PhIAT's capability in analyzing both ideal and skewed clusters, supporting troubleshooting and analysis throughout the implementation process. Phase-imaging opens new avenues for exploration by exceeding the precision attainable with TOF-ICR; with the advancements made in this work towards implementation at TITAN, explorations beyond the Standard Model come within reach. Finally, with the addition of the PI-ICR timing scheme into the MPET DAQ, TITAN is one step closer to implementing phase-imaging for precision mass measurements, with both TOF-ICR and PI-ICR measurement modes now available.

Chapter 6

Conclusion

Mass measurements are critical in shaping our understanding of the forces that govern nature, the origin of heavy elements in our universe, and the structure of exotic nuclei. Recent advancements in experimental nuclear physics have allowed us to investigate the universe on some of the smallest scales with precision, adding to our collective understanding of its inner workings and pushing the limits of the unknown.

The TITAN facility at TRIUMF in Vancouver, Canada exemplifies the forefront of scientific exploration and the demonstrated precision and accuracy of measurements have established it as a leader in experimental nuclear physics.

The mass determinations [1] presented in this work further confirms our capability for both precision and accuracy. With precisions ≤ 50 keV and in excellent agreement with prior measurements, the tin measurements presented herein add to the ever-growing evidence of typical mid-shell behaviour as described in the nuclear shell model. This was observed from the S_{2n} surface, wherein a near linear trend was observed for the measured nuclides. Based on the rates detected in this experiment and previous success with much lower rates, the low rates expected as we near the dripline are within the sensitivity range of the device. Therefore, this experiment shows TITAN's capacity to realize the measurement of doubly magic ${}^{100}_{50}Sn_{50}$. Moreover, the first direct measurements of ${}^{89}Zr$ and ${}^{90,91}Y$ assure the accuracy to make them calibrants for experiments hereafter. The simultaneous measurement of Sn^+ with ZrO^+ and YO^+ showcase one the many advantages of the MR-TOF MS technique: its broadband capability. This ability enables precision measurements of the not only ions of interest but the other isobaric nuclides which may be of interest in and of themselves, as illustrated in this work.

The second focus of this thesis was the ongoing implementation of the Phase-Image Ion-Cyclotron-Resonance (PI-ICR) technique at TITAN. The technique will allow TITAN to achieve precisions in Penning trap mass spectrometry of order 10^{-10}, as is needed for the

most stringent tests of the Standard Model. For this purpose, the data acquisition system now includes the necessary timing scheme to permit the measurement of the cyclotron frequency by varying its phase through a user-defined time. In addition, the work presented herein improves the on-line data analysis of PI-ICR measurements. Easy, fast, and reliable access to this information is equally important during the implementation and experimental preparations to find and to eliminate systematic errors, such as non-zero initial radial motion. During the experiment itself, on-line analysis is crucial in identifying the presence of contaminants and separating them from the ion of interest through the phase-accumulation time. As such, the upgrades described to the Phase-Imaging Analysis Tool, which was fully tested through simulated data, and the integration of the new timing scheme in the DAQ are crucial steps towards the full implementation of PI-ICR technique at TITAN.

This thesis showcases the measurement and the development sides of ion-trap-based mass spectrometry. The mass measurements presented reinforce our understanding of shell structure evolution from stable nuclei towards the nuclear driplines and the nuclear shell model for mid-shell nuclides. Moreover, the direct measurements anchor chains of indirect and extrapolated mass surfaces by providing an accurate reference point. With the integration of the PI-ICR technique, supported by the upgrades discussed in this work, new investigations into fundamental physics and physics beyond the Standard Model become possible, such as the breaking of CKM unitarity. This opens avenues for deeper insights into the science governing our universe.

The work presented in this thesis illustrates the strides nuclear science has made over the past 200 years, from firing alpha particles at metal sheets to conducting experiments with precisions as fine as one part per billion. Each leap forward, built on the efforts of scientists past, brings us closer to formulating the fundamental laws of nature. The contributions of individuals toward a greater collective understanding of the universe reflects the stardust within us all and our shared desire to understand ourselves and our place in the continuum.

Bibliography

[1] A. Czihaly, S. Beck, J. Bergmann, C. L. Brown, T. Brunner, T. Dickel, J. Dilling, E. Dunling, J. Flowerdew, Z. Hockenbery, A. Jacobs, B. Kootte, S. Malbrunot-Ettenauer, F. M. Millán, A. Mollaebrahimi, E. Leistenschneider, E. M. Lykiardopoulou, I. Mukul, S. F. Paul, W. R. Plaß, M. P. Reiter, C. Scheidenberger, J. James L. Tracy, and A. A. Kwiatkowski, "Exploring the Western Shoreline of the Nuclear Chart: What Precision Mass Spectrometry with TITAN-TRIUMF Can Teach Us About Nuclear Existence," *Preprints*, 2024.

[2] K. Hentschel, *Atomic Models, J.J. Thomson's "Plum Pudding" Model*, pp. 18–21. Berlin, Heidelberg: Springer Berlin Heidelberg, 2009.

[3] H. Geiger, E. Marsden, and E. Rutherford, "On a Diffuse Reflection of the α-Particles," *Proceedings of the Royal Society of London. Series A, Containing Papers of a Mathematical and Physical Character*, vol. 82, no. 557, pp. 495–500, 1909.

[4] E. Rutherford, "The Scattering of α and β Particles by Matter and the Structure of the Atom," *The London, Edinburgh, and Dublin Philosophical Magazine and Journal of Science*, vol. 21, no. 125, pp. 669–688, 1911.

[5] A. Van den Broek, "The Number of Possible Elements and Mendeléff's "Cubic" Periodic System," *Nature*, vol. 87, no. 2177, pp. 78–78, 1911.

[6] H. Moseley, "The High-frequency Spectra of the Elements," *The London, Edinburgh, and Dublin Philosophical Magazine and Journal of Science*, vol. 26, no. 156, pp. 1024–1034, 1913.

[7] N. Bohr, "On the Constitution of Atoms and Molecules," *The London, Edinburgh, and Dublin Philosophical Magazine and Journal of Science*, vol. 26, no. 151, pp. 1–25, 1913.

[8] W. Bothe and H. Becker, "Künstliche Erregung von Kern-γ-Strahlen," *Zeitschrift für Physik*, vol. 66, no. 5, pp. 289–306, 1930.

[9] J. Chadwick, "Possible Existence of a Neutron," *Nature*, vol. 129, no. 3252, pp. 312–312, 1932.

[10] G. Gamow and E. Rutherford, "Mass Defect Curve and Nuclear Constitution," *Proceedings of the Royal Society of London. Series A, Containing Papers of a Mathematical and Physical Character*, vol. 126, no. 803, pp. 632–644, 1930.

[11] C. F. V. Weizsäcker, "Zur Theorie der Kernmassen," *Zeitschrift für Physik*, vol. 96, no. 7, pp. 431–458, 1935.

[12] K. Blaum, "High-Accuracy Mass Spectrometry with Stored Ions," *Physics Reports10.Dr*, vol. 42520, 2006.

[13] "The Nobel Prize in Physics 1963 — nobelprize.org." https://www.nobelprize.org/prizes/physics/1963/summary/.

[14] C. Thibault, R. Klapisch, C. Rigaud, A. M. Poskanzer, R. Prieels, L. Lessard, and W. Reisdorf, "Direct Measurement of the Masses of ^{11}Li and $^{26-32}$Na with an On-Line Mass Spectrometer," *Phys. Rev. C*, vol. 12, pp. 644–657, 1975.

[15] T. Otsuka, A. Gade, O. Sorlin, T. Suzuki, and Y. Utsuno, "Evolution of Shell Structure in Exotic Nuclei," *Rev. Mod. Phys.*, vol. 92, p. 015002, 2020.

[16] J. Carlson, M. P. Carpenter, R. Casten, C. Elster, P. Fallon, A. Gade, C. Gross, G. Hagen, A. C. Hayes, D. W. Higinbotham, C. R. Howell, C. J. Horowitz, K. L. Jones, F. G. Kondev, S. Lapi, A. Macchiavelli, E. A. McCutchen, J. Natowitz, W. Nazarewicz, T. Papenbrock, S. Reddy, M. A. Riley, M. J. Savage, G. Savard, B. M. Sherrill, L. G. Sobotka, M. A. Stoyer, M. Betty Tsang, K. Vetter, I. Wiedenhoever, A. H. Wuosmaa, and S. Yennello, "white Paper on Nuclear Astrophysics and Low-Energy Nuclear Physics, Part 2: Low-Energy Nuclear Physics," *Progress in Particle and Nuclear Physics*, vol. 94, pp. 68–124, 2017.

[17] A. Ekström, C. Forssén, G. Hagen, G. R. Jansen, W. Jiang, and T. Papenbrock, "What is ab initio in nuclear theory?," *Frontiers in Physics*, vol. 11, 2023.

[18] J. Dilling, K. Blaum, M. Brodeur, and S. Eliseev, "Penning-Trap Mass Measurements in Atomic and Nuclear Physics," *Ann. Rev. Nucl. Part. Sci.*, vol. 68, pp. 45–74, 2018.

[19] W. Huang, M. Wang, F. Kondev, G. Audi, and S. Naimi, "The AME 2020 Atomic Mass Evaluation (I). Evaluation of Input Data, and Adjustment Procedures," *Chinese Physics C*, vol. 45, no. 3, p. 030002, 2021.

[20] B. Jonson, "Light Dripline Nuclei," *Physics Reports*, vol. 389, no. 1, pp. 1–59, 2004.

[21] P. G. Hansen, A. S. Jensen, and B. Jonson, "Nuclear Halos," *Ann. Rev. Nucl. Part. Sci.*, vol. 45, pp. 591–634, 1995.

[22] A. A. Kwiatkowski, J. Dilling, S. Malbrunot-Ettenauer, and M. P. Reiter, "15 Years of Precision Mass Measurements at TITAN," *The European Physical Journal A*, vol. 60, no. 4, p. 87, 2024.

[23] J. C. Hardy and I. S. Towner, "Superallowed $0^+ \rightarrow 0^+$ Nuclear β Decays: 2020 Critical Survey, with Implications for V_{ud} and CKM Unitarity," *Phys. Rev. C*, vol. 102, p. 045501, 2020.

[24] F. W. Aston, "Mass Spectra and Isotopes." Nobel Lecture, 1922.

[25] "The Nobel Prize in Chemistry 1922 — nobelprize.org." https://www.nobelprize.org/prizes/chemistry/1922/summary/.

[26] F. Bosch, "Storage Rings for Radioactive, Highly Charged Ions," *Nuclear Physics A*, vol. 701, no. 1, pp. 509–515, 2002. 5th International Conference on Radioactive Nuclear Beams.

[27] "eSR — gsi.de." https://www.gsi.de/en/work/research/appamml/atomic_physics/experimental_facilities/esr.

[28] Z. Meisel and S. George, "Time-of-Flight Mass Spectrometry of Very Exotic Systems," *International Journal of Mass Spectrometry*, vol. 349-350, pp. 145–150, 2013.

[29] M. P. Reiter, S. A. S. Andrés, J. Bergmann, T. Dickel, J. Dilling, A. Jacobs, A. A. Kwiatkowski, W. Plaß, C. Scheidenberger, D. Short, C. Will, C. Babcock, E. Dunling, A. Finlay, C. Hornung, C. Jesch, R. Klawitter, B. Kootte, D. Lascar, E. Leistenschneider, T. Murböck, S. Paul, and M. Yavor, "Commissioning and Performance of TITAN's Multiple-Reflection Time-of-Flight Mass-Spectrometer and Isobar Separator," *Nuclear Instruments and Methods in Physics Research Section A: Accelerators, Spectrometers, Detectors and Associated Equipment*, vol. 1018, p. 165823, 2021.

[30] "The Nobel Prize in Physics 1989 — nobelprize.org." https://www.nobelprize.org/prizes/physics/1989/summary/.

[31] M. König, G. Bollen, H.-J. Kluge, T. Otto, and J. Szerypo, "Quadrupole Excitation of Stored Ion Motion at the True Cyclotron Frequency," *International Journal of Mass Spectrometry and Ion Processes*, vol. 142, no. 1, pp. 95–116, 1995.

[32] S. Eliseev, K. Blaum, M. Block, C. Droese, M. Goncharov, E. Minaya Ramirez, D. A. Nesterenko, Y. N. Novikov, and L. Schweikhard, "phase-Imaging Ion-Cyclotron-Resonance Measurements for Short-Lived Nuclides," *Phys. Rev. Lett.*, vol. 110, p. 082501, 2013.

[33] M. Smith, M. Brodeur, T. Brunner, S. Ettenauer, A. Lapierre, R. Ringle, V. L. Ryjkov, F. Ames, P. Bricault, G. W. F. Drake, P. Delheij, D. Lunney, F. Sarazin, and J. Dilling, "First Penning-Trap Mass Measurement of the Exotic Halo Nucleus ^{11}Li," *Phys. Rev. Lett.*, vol. 101, p. 202501, 2008.

[34] P. G. Bricault, F. Ames, M. Dombsky, P. Kunz, and J. Lassen, *Rare Isotope Beams at ISAC-Target and Ion Source Systems*, pp. 25–49. Dordrecht: Springer Netherlands, 2014.

[35] A. Sen, F. Ames, P. Bricault, J. Lassen, A. Laxdal, and A. Mjos, "Extraction and Low Energy Beam Transport from a Surface Ion Source at the TRIUMF-ISAC Facility," *Nuclear Instruments and Methods in Physics Research Section B: Beam Interactions with Materials and Atoms*, vol. 376, pp. 97–101, 2016.

[36] M. Mostamand, R. Li, J. Romans, F. Ames, P. Kunz, A. Mjs, and J. Lassen, "Production of Clean Rare Isotope Beams at TRIUMF Ion Guide Laser Ion Source," *Hyperfine Interactions*, vol. 241, no. 1, p. 36, 2020.

[37] J. Lassen, R. Li, M. Mostamand, A. Gacsbaranyi, P. Kunz, C. Babcock, D. Bishop, A. Teigelhöfer, F. Ames, and A. Gottberg, "Developments at TRIUMF's Laser Resonance Ionization Ion Source and Multi-Element Operation," *Nuclear Instruments and Methods in Physics Research Section B: Beam Interactions with Materials and Atoms*, vol. 541, pp. 137–140, 2023.

[38] B. Schultz, F. Ames, O. Kester, P. Kunz, A. Mjøs, and J. Sandor, "FEBIAD Ion Source Development at TRIUMF-ISAC," in *Proc. 9th International Particle Accelerator*

Conference 2018, no. 9 in International Particle Accelerator Conference, pp. 4730–4733, JACW Publishing, 2018. https://doi.org/10.18429/JACoW-IPAC2018-THPML041.

[39] N. Avreline, T. Au, C. Bartlett, I. Bylinskii, B. Jakovljevic, and V. Zvyagintsev, "Operation and Maintenance of RF System of 520 MeV TRIUMF Cyclotron," 2017.

[40] T. Brunner, M. Smith, M. Brodeur, S. Ettenauer, A. Gallant, V. Simon, A. Chaudhuri, A. Lapierre, E. Mané, R. Ringle, M. Simon, J. Vaz, P. Delheij, M. Good, M. Pearson, and J. Dilling, "TITAN's Digital RFQ Ion Beam Cooler and Buncher, Operation and Performance," *Nuclear Instruments and Methods in Physics Research Section A: Accelerators, Spectrometers, Detectors and Associated Equipment*, vol. 676, pp. 32–43, 2012.

[41] C. Jesch, T. Dickel, W. R. Plaß, D. Short, S. Ayet San Andres, J. Dilling, H. Geissel, F. Greiner, J. Lang, K. G. Leach, W. Lippert, C. Scheidenberger, and M. I. Yavor, "The MR-TOF-MS Isobar Separator for the TITAN Facility at TRIUMF," *Hyperfine Interactions*, vol. 235, no. 1, pp. 97–106, 2015.

[42] E. Leistenschneider, M. P. Reiter, S. Ayet San Andrés, B. Kootte, J. D. Holt, P. Navrátil, C. Babcock, C. Barbieri, B. R. Barquest, J. Bergmann, J. Bollig, T. Brunner, E. Dunling, A. Finlay, H. Geissel, L. Graham, F. Greiner, H. Hergert, C. Hornung, C. Jesch, R. Klawitter, Y. Lan, D. Lascar, K. G. Leach, W. Lippert, J. E. McKay, S. F. Paul, A. Schwenk, D. Short, J. Simonis, V. Somà, R. Steinbrügge, S. R. Stroberg, R. Thompson, M. E. Wieser, C. Will, M. Yavor, C. Andreoiu, T. Dickel, I. Dillmann, G. Gwinner, W. R. Plaß, C. Scheidenberger, A. A. Kwiatkowski, and J. Dilling, "Dawning of the $N = 32$ Shell Closure Seen Through Precision Mass Measurements of Neutron-Rich Titanium Isotopes," *Phys. Rev. Lett.*, vol. 120, p. 062503, 2018.

[43] T. Dickel, W. Plaß, A. Becker, U. Czok, H. Geissel, E. Haettner, C. Jesch, W. Kinsel, M. Petrick, C. Scheidenberger, A. Simon, and M. Yavor, "A High-Performance Multiple-Reflection Time-of-Flight Mass Spectrometer and Isobar Separator for the Research with Exotic Nuclei," *Nuclear Instruments and Methods in Physics Research Section A: Accelerators, Spectrometers, Detectors and Associated Equipment*, vol. 777, pp. 172–188, 2015.

[44] M. I. Yavor, W. R. Plaß, T. Dickel, H. Geissel, and C. Scheidenberger, "Ion-Optical Design of a High-Performance Multiple-Reflection Time-of-Flight Mass Spectrometer

and Isobar Separator," *International Journal of Mass Spectrometry*, vol. 381-382, pp. 1–9, 2015.

[45] W. R. Plaß, T. Dickel, U. Czok, H. Geissel, M. Petrick, K. Reinheimer, C. Scheidenberger, and M. I.Yavor, "Isobar Separation by Time-of-Flight Mass Spectrometry for Low-Energy Radioactive Ion Beam Facilities," *Nuclear Instruments and Methods in Physics Research Section B: Beam Interactions with Materials and Atoms*, vol. 266, no. 19, pp. 4560–4564, 2008.

[46] S. Ayet San Andrés, C. Hornung, J. Ebert, W. R. Plaß, T. Dickel, H. Geissel, C. Scheidenberger, J. Bergmann, F. Greiner, E. Haettner, C. Jesch, W. Lippert, I. Mardor, I. Miskun, Z. Patyk, S. Pietri, A. Pihktelev, S. Purushothaman, M. P. Reiter, A.-K. Rink, H. Weick, M. I. Yavor, S. Bagchi, V. Charviakova, P. Constantin, M. Diwisch, A. Finlay, S. Kaur, R. Knöbel, J. Lang, B. Mei, I. D. Moore, J.-H. Otto, I. Pohjalainen, A. Prochazka, C. Rappold, M. Takechi, Y. K. Tanaka, J. S. Winfield, and X. Xu, "High-Resolution, Accurate Multiple-Reflection Time-of-Flight Mass Spectrometry for Short-Lived, Exotic Nuclei of a Few Events in their Ground and Low-Lying Isomeric States," *Phys. Rev. C*, vol. 99, p. 064313, 2019.

[47] C. Jesch, *The Multiple-Reflection Time-of-Flight Isobar Separator for TITAN and Direct Mass Measurements at the FRS Ion Catcher*. PhD thesis, Justus-Liebig-Universitat Gießen, 2016.

[48] S. Beck, B. Kootte, I. Dedes, T. Dickel, A. A. Kwiatkowski, E. M. Lykiardopoulou, W. R. Plaß, M. P. Reiter, C. Andreoiu, J. Bergmann, T. Brunner, D. Curien, J. Dilling, J. Dudek, E. Dunling, J. Flowerdew, A. Gaamouci, L. Graham, G. Gwinner, A. Jacobs, R. Klawitter, Y. Lan, E. Leistenschneider, N. Minkov, V. Monier, I. Mukul, S. F. Paul, C. Scheidenberger, R. I. Thompson, J. L. Tracy, M. Vansteenkiste, H.-L. Wang, M. E. Wieser, C. Will, and J. Yang, "Mass Measurements of Neutron-Deficient Yb Isotopes and Nuclear Structure at the Extreme Proton-Rich Side of the $N = 82$ Shell," *Phys. Rev. Lett.*, vol. 127, p. 112501, 2021.

[49] T. Dickel, W. R. Plaß, W. Lippert, J. Lang, M. I. Yavor, H. Geissel, and C. Scheidenberger, "Isobar Separation in a Multiple-Reflection Time-of-Flight Mass Spectrometer by Mass-Selective Re-Trapping," *Journal of the American Society for Mass Spectrometry*, 2017.

[50] S. F. Paul, J. Bergmann, J. D. Cardona, K. A. Dietrich, E. Dunling, Z. Hockenbery, C. Hornung, C. Izzo, A. Jacobs, A. Javaji, B. Kootte, Y. Lan, E. Leistenschneider, E. M. Lykiardopoulou, I. Mukul, T. Murböck, W. S. Porter, R. Silwal, M. B. Smith, J. Ringuette, T. Brunner, T. Dickel, I. Dillmann, G. Gwinner, M. MacCormick, M. P. Reiter, H. Schatz, N. A. Smirnova, J. Dilling, and A. A. Kwiatkowski, "Mass Measurements of $^{60–63}$Ga Reduce X-Ray Burst Model Uncertainties and Extend the Evaluated $T = 1$ Isobaric Multiplet Mass Equation," *Phys. Rev. C*, vol. 104, p. 065803, 2021.

[51] A. Lapierre, M. Brodeur, T. Brunner, S. Ettenauer, A. Gallant, V. Simon, M. Good, M. Froese, J. Crespo López-Urrutia, P. Delheij, S. Epp, R. Ringle, S. Schwarz, J. Ullrich, and J. Dilling, "The TITAN EBIT Charge Breeder for Mass Measurements on Highly Charged Short-Lived Isotopes—First Online Operation," *Nuclear Instruments and Methods in Physics Research Section A: Accelerators, Spectrometers, Detectors and Associated Equipment*, vol. 624, no. 1, pp. 54–64, 2010.

[52] Ludwig Maximilian University of Munich, "Penning Traps." https://www.med.physik.uni-muenchen.de/research/nuclear-science/nuclear-masses/mlltrap/layout/traps/index.html.

[53] A. A. Kwiatkowski, T. Brunner, J. D. Holt, A. Chaudhuri, U. Chowdhury, M. Eibach, J. Engel, A. T. Gallant, A. Grossheim, M. Horoi, A. Lennarz, T. D. Macdonald, M. R. Pearson, B. E. Schultz, M. C. Simon, R. A. Senkov, V. V. Simon, K. Zuber, and J. Dilling, "New Determination of Double-β-Decay Properties in 48Ca: High-Precision Q-Value Measurement and Improved Nuclear Matrix Element Calculations," *Physical Review C*, vol. 89, no. 4, 2014.

[54] E. Leistenschneider, R. Klawitter, A. Lennarz, M. Alanssari, J. C. Bale, B. R. Barquest, U. Chowdhury, A. Finlay, A. T. Gallant, B. Kootte, D. Lascar, K. G. Leach, A. J. Mayer, D. Short, C. Andreoiu, G. Gwinner, M. E. Wieser, J. Dilling, and A. A. Kwiatkowski, "Diversifying Beam Species Through Decay and Recapture Ion Trapping: A Demonstrative Experiment at TITAN-EBIT," *Journal of Physics G: Nuclear and Particle Physics*, vol. 47, no. 4, p. 045113, 2020.

[55] J. Lassen, P. Bricault, M. Dombsky, J. P. Lavoie, M. Gillner, T. Gottwald, F. Hellbusch, A. Teigelhöfer, A. Voss, and K. D. A. Wendt, "Laser Ion Source Operation at the TRIUMF Radioactive Ion Beam Facility," *AIP Conference Proceedings*, vol. 1104, no. 1, pp. 9–15, 2009.

[56] "TRIUMF-ISAC Target Station and Mass Separator Commissioning," *Nuclear Physics A*, vol. 701, no. 1, pp. 49–53, 2002.

[57] T. Dickel, S. San Andres, S. Beck, J. Bergmann, J. Dilling, F. Greiner, C. Hornung, A. Jacobs, G. Kripko-Koncz, A. Kwiatkowski, E. Leistenschneider, A. Pikthtelev, W. Plaß, M. Reiter, C. Scheidenberger, and C. Will, "Recent Upgrades of the Multiple-Reflection Time-of-Flight Mass Spectrometer at TITAN, TRIUMF," *Hyperfine Interactions*, vol. 240, 2019.

[58] E. Leistenschneider, *Dawning Of nuclear Magicity in N = 32 Seen Through Precision Mass Spectrometry*. PhD thesis, University of British Columbia, 2019.

[59] S. F. Paul, "EMGFit - Fitting of Time-of-Flight Mass Spectra with Hyper-EMG Models," 2024.

[60] M. Wang, W. Huang, F. Kondev, G. Audi, and S. Naimi, "The AME 2020 Atomic Mass Evaluation (II). Tables, Graphs and References," *Chinese Physics C*, vol. 45, no. 3, p. 030003, 2021.

[61] M. P. Reiter, S. Ayet San Andrés, E. Dunling, B. Kootte, E. Leistenschneider, C. Andreoiu, C. Babcock, B. R. Barquest, J. Bollig, T. Brunner, I. Dillmann, A. Finlay, G. Gwinner, L. Graham, J. D. Holt, C. Hornung, C. Jesch, R. Klawitter, Y. Lan, D. Lascar, J. E. McKay, S. F. Paul, R. Steinbrügge, R. Thompson, J. L. Tracy, M. E. Wieser, C. Will, T. Dickel, W. R. Plaß, C. Scheidenberger, A. A. Kwiatkowski, and J. Dilling, "Quenching of the $N = 32$ Neutron Shell Closure Studied via Precision Mass Measurements of Neutron-Rich Vanadium Isotopes," *Phys. Rev. C*, vol. 98, p. 024310, 2018.

[62] V. Elomaa, G. K. Vorobjev, A. Kankainen, L. Batist, S. Eliseev, T. Eronen, J. Hakala, A. Jokinen, I. D. Moore, Y. N. Novikov, H. Penttilä, A. Popov, S. Rahaman, J. Rissanen, A. Saastamoinen, H. Schatz, D. M. Seliverstov, C. Weber, and J. Äystö, "Quenching of the SnSbTe Cycle in the RP Process," *Phys. Rev. Lett.*, vol. 102, p. 252501, 2009.

[63] A. Martin, D. Ackermann, G. Audi, K. Blaum, M. Block, A. Chaudhuri, Z. Di, S. Eliseev, R. Ferrer, D. Habs, F. Herfurth, F. Heßberger, S. Hofmann, H. Kluge, M. Mazzocco, M. Mukherjee, J. Neumayr, Y. Novikov, W. Plaß, and C. Weber, "Mass Measurements of Neutron-Deficient Radionuclides Near the End-Point of the RP-Process with SHIPTRAP," *European Physical Journal A*, vol. 34, pp. 341–348, 2007.

[64] R. Barden, R. Kirchner, O. Klepper, A. Plochocki, G. E. Rathke, E. Roeckl, K. Rykaczewski, D. Schardt, and J. Zylicz, "The Gamow-Teller β-Decay of Neutron-Deficient Even Isotopes of Tin," *European Physical Journal A*, vol. 329, no. 3, pp. 319–330, 1988.

[65] H. Keller, R. Kirchner, O. Klepper, E. Roeckl, D. Schardt, R. S. Simon, P. Kleinheinz, R. Menegazzo, C. F. Liang, P. Paris, K. Rykaczewski, and J. Żylicz, "β-Endpoint Measurements Near ^{100}Sn and ^{146}Gd," *Zeitschrift für Physik A Hadrons and Nuclei*, vol. 340, no. 4, pp. 363–370, 1991.

[66] M. G. Mayer, "On Closed Shells in Nuclei," *Phys. Rev.*, vol. 75, pp. 1969–1970, 1949.

[67] P. Hoff, K. Aleklett, E. Lund, and G. Rudstam, "Decay Schemes and Total Decay Energies of ^{89}Br and ^{90}Br," *Zeitschrift für Physik A Atoms and Nuclei*, vol. 300, no. 4, pp. 289–298, 1981.

[68] S. Rahaman, U. Hager, V. Elomaa, T. Eronen, J. Hakala, A. Jokinen, A. Kankainen, P. Karvonen, I. D. Moore, H. Penttilä, S. Rinta-Antila, J. Rissanen, A. Saastamoinen, T. Sonoda, and J. Äystö, "Precise Atomic Masses of Neutron-Rich Br and Rb Nuclei Close to the R-Process Path," *The European Physical Journal A*, vol. 32, no. 1, pp. 87–96, 2007.

[69] P. Delahaye, G. Audi, K. Blaum, F. Carrel, S. George, F. Herfurth, A. Herlert, A. Kellerbauer, H.-J. Kluge, D. Lunney, L. Schweikhard, and C. Yazidjian, "High-Accuracy Mass Measurements of Neutron-Rich Kr Isotopes," *Phys. Rev. C*, vol. 74, p. 034331, 2006.

[70] L. S. Brown and G. Gabrielse, "Geonium Theory: Physics of a Single Electron or Ion in a Penning Trap," *Rev. Mod. Phys.*, vol. 58, pp. 233–311, 1986.

[71] R. Ringle, G. Bollen, A. Prinke, J. Savory, P. Schury, S. Schwarz, and T. Sun, "A "Lorentz" Steerer for Ion Injection into a Penning Trap," *International Journal of Mass Spectrometry*, vol. 263, no. 1, pp. 38–44, 2007.

[72] G. Bollen, "Mass Measurements of Short-Lived Nuclides with Ion Traps," *Nuclear Physics A*, vol. 693, no. 1, pp. 3–18, 2001.

[73] S. Eliseev, K. Blaum, M. Block, A. Dörr, C. Droese, T. Eronen, M. Goncharov, M. Höcker, J. Ketter, E. M. Ramirez, D. A. Nesterenko, Y. N. Novikov, and L. Schweikhard, "A Phase-Imaging Technique for Cyclotron-Frequency Measurements," *Applied Physics B: Lasers and Optics*, vol. 114, no. 1-2, pp. 107–128, 2014.

[74] RoentDek, "MCP Delay Line Detector Manual." https://www.roentdek.com/manuals/MCP%20Delay%20Line%20manual.pdf, 2024.

[75] E. M. Lykiardopoulou, C. Izzo, E. Leistenschneider, A. A. Kwiatkowski, and J. Dilling, "Towards High Precision Mass Measurements of Highly Charged Ions Using the Phase-Imaging Ion-Cyclotron-Resonance Technique at TITAN," *Hyperfine Interactions*, vol. 241, no. 1, p. 37, 2020.

[76] A. Czihaly, "PhIAT Download." https://github.com/TITANCollaboration/phiat, 2024.

[77] D. Comaniciu and P. Meer, "Mean Shift: A Robust Approach Toward Feature Space Analysis," *IEEE Transactions on Pattern Analysis and Machine Intelligence*, vol. 24, no. 5, pp. 603–619, 2002.

[78] W. Porter, *The Northern Shore of the N = 40 Island of Inversion Through Precision Mass Measurements and Developments Towards Phase-Imaging Ion-Cyclotron-Resonance at the TITAN MPET*. PhD thesis, University of British Columbia, 2021.

[79] R. Orford, *A Phase-Imaging Technique For Precision Mass Measurements Of Neutron-Rich Nuclei With The Canadian Penning Trap Mass Spectrometer*. PhD thesis, University of McGill, 2018.

[80] A. Czihaly, "PhIAT Documentation." https://phiat-documentation.readthedocs.io/en/latest/, 2024.

[81] TRIUMF, "MIDAS Data Aquisition Software." https://daq00.triumf.ca/MidasWiki/index.php/Main_Page#Documentation, 2013.

[82] Argonne National Laboratory, "EPICS Control System." https://epics.anl.gov/, 1993.

[83] D. Ray, G. Savard, J. Clark, R. Orford, K. Sharma, A. Valverde, M. Brodeur, D. Burdette, N. Callahan, B. Liu, S. Marley, G. Morgan, L. Varriano, G. Wilson, and X. Yan, *Precision Mass Measurements of Neutron-Rich Nuclides Using the Canadian Penning Trap Mass Spectrometer for Studying the Astrophysical R Process*. PhD thesis, 2021.

Appendix A

Appendix

A.1 PhIAT's Tool for Ion Phase Simulation (TIPS)

PhIAT's Tool for Ion Phase Simulation (TIPS) is written and executed using MATLAB, with brief instructions and the full code available in Appendix A.1.1. TIPS works by iterating through each given accumulation time (t_{acc}) and, in a nested loop, each input cyclotron frequency, to determine the phase evolution, ϕ. Next, the Cartesian x and y coordinates are determined from the phase and user-specified radius, R. Positional data is created with a Gaussian distribution centered around x and y with the standard deviation specified by $x_{\text{pos\_deviation}}$ and $y_{\text{pos\_deviation}}$, respectively. Similarly, TOF data is centered around the user-specified TOF with the standard deviation given by $TOF_{\text{deviation}}$. TIPS then determines the reference phase i.e. the cycle in which the phase is not evolved. Similarly to what is described above, the Cartesian coordinates are generated. Lastly, TIPS creates a data file containing the generated data.

The user inputs of TIPS are:

- t_acc_list: A list of accumulation times, in units of seconds (s). One file will be created for each item in this list.
- File_name: The directory where the data files will saved to.
- spot_freq_list: A list of cyclotron frequencies for the spots to be simulated, in units of Hertz (Hz).
- R: Average distance from the trap center to the spots, in units of milimeters (mm).
- x_pos_deviation: Gaussian spread of x position.
- y_pos_deviation: Gaussian spread of y position.

- TOF: Mean of Gaussian distribution for time-of-flight.
- tof_deviation: Gaussian spread of time(s) of flight.
- counts_per_spot: Counts to be generated for each spot.
- omega_minus: Magnetron frequency in the trap, in units of Hertz (Hz).
- ref_phase: Reference spot (t_acc = 0) phase.
- amp: Amplitude of the sinusoid dependence. This quantity is irrelevant for TITAN so it has been set to 0.0. This functionality has not been removed to make it accessible to other facilities.
- phase_const: Phase constant of the sinusoid dependence. This quantity is irrelevant for TITAN so it has been set to 0.0. This functionality has not been removed to make it accessible to other facilities.

The output of TIPS are two types of comma separated value (.csv) files:

- File(s) containing simulated x and y positions, time of flight, and (faux) time to digital converter trigger information. One file is created for each specified accumulation time, t_acc.
- File_list: Contains the directories of simulated data files, associated accumulation times, t_acc, and reference file assignments.

The following are the TIPS settings used for the generated symmetric and asymmetric clusters:

- $t_{\text{acc}} = 0.1, 0.3, 0.5$ s
- $\nu_c = 1.457$ Hz
- $R = 4$ mm
- $TOF = 0.000006$ s
- $TOF_{\text{deviation}} = 0.000003$ s
- counts per spot = 250
- $\nu_- = 6150$ Hz

- $\phi_{\text{ref}} = 180°$

TIPS settings to create symmetric clusters:

- x_pos_deviation = 0.3 mm
- y_pos_deviation = 0.3 mm

TIPS settings to create asymmetric clusters:

- x_pos_deviation = 1 mm
- y_pos_deviation = 0.2 mm

A.1.1 TIPS Code

The following is the MATLAB code for the generation of simulated data.

```
%% TIPS.m
%
% Welcome to the Tool for Ion Position Simulation (TIPS)!
%
% Language: MATLAB
%
% Created by Sam Porter
% University of British Columbia, TRIUMF
%
% Updated by Annabelle Czihaly
% University of Victoria, TRIUMF
%
% last updated on 11/10/2024
%
%% User Inputs %%

% From Self-Generated Tacc List %%

clearvars

tacc_list = [.600030,.6000479,.6000658]; % List of Accumulation Times
```

```
new_filename = '\Users\aczihaly\Documents\PIICR_Analysis\Data\Simulated\3_symmetric_spot

spot_freq_list = [1444409.260, 1444391.967,1444388.117]; % Expected w_c of spots in the
R = 4; % Average radius of spots, in mm
x_pos_deviation = 0.5; % Sigma of Gaussian distribution for X positions
y_pos_deviation = 0.5; % Sigma of Gaussian distribution for Y positions
TOF = 0.000006; % Mean of Gaussian distribution for time-of-flight
tof_deviation = 0.000003 % Sigma of Guassian distribution for time-of-flight

counts_per_spot = 250;
w_minus = 6150; % Taken from 2021 TITAN spreadsheet for 85Rb
ref_phase = 180; % Phase of Reference Spot
amp = 0.0; % Amplitude of Sine Dependency, TITAN USERS LEAVE AS 0
phase_const = 0; % Phase Constant of Sine Dependency, TITAN USERS LEAVE AS 0

% NOTE: TRAP CENTER IS TREATED AS (0,0)
%% Code Body %%

% Determine Number of Actual vs. Ref Files %%

ctr = 0;
for object = tacc_list
    if object > 0
        ctr = ctr + 1;
    end
end

tacc_list = tacc_list(1:ctr);

data_filename_list = {};
ref_phase = ref_phase*pi/180;

ii = 1;
```

```
% From Tacc & w_c Determine X/Y %%

for i = tacc_list
    x_data = [];
    y_data = [];
    TOF_data = [];
    trigger_data = [];

    for j = spot_freq_list
        w_c_sin_shifted = j + amp*sin((2*pi*w_minus)*i + phase_const); % Sine dependence
        phase_i = 2*pi*i*w_c_sin_shifted + ref_phase;

        if phase_i > pi
            phase_i = phase_i - 2*pi;
        end

        x = R*cos(phase_i); % NOTE: we're shifting the phase but not the radius, which m
        y = R*sin(phase_i);

        for k = 1:counts_per_spot % For the number of points per spot, generate data wit
            x_data = cat(1,x_data,random('Normal',x,x_pos_deviation));
            y_data = cat(1,y_data,random('Normal',y,y_pos_deviation));
            TOF_data = cat(1,TOF_data,random('Normal',TOF,tof_deviation));
            trigger_data = cat(1,trigger_data,k+random('Uniform',0,1));
        end

    end

    % Write New Data File %%

    file_data = cat(2,x_data,y_data,TOF_data,trigger_data);
    data_filename = strcat(new_filename,num2str(i),'.csv');
    dlmwrite(data_filename,file_data)

    data_filename_list{ii,1} = data_filename;
```

```
    ii = ii + 1;
end

% Write New Reference Data File %%

if ref_phase > pi
    ref_phase = ref_phase - 2*pi;
end

x = R*cos(ref_phase);
y = R*sin(ref_phase);

x_data = [];
y_data = [];
TOF_data = [];
trigger_data = [];

for k = 1:counts_per_spot
    x_data = cat(1,x_data,random('Normal',x,x_pos_deviation));
    y_data = cat(1,y_data,random('Normal',y,y_pos_deviation));
    TOF_data = cat(1,TOF_data,random('Normal',TOF,tof_deviation));
    trigger_data = cat(1,trigger_data,k+random('Uniform',0,1));
end

file_data = cat(2,x_data,y_data,TOF_data,trigger_data);
data_filename = strcat(new_filename,'ref.csv');
dlmwrite(data_filename,file_data)

% Construct List of Files .csv %%

final_filename_list = {};
ii = 1;

while ii <= ctr
```

```
    final_filename_list{ii,1} = data_filename_list{ii,:};

    ii = ii + 1;
end

final_filename_list{ctr+1,1} = data_filename;

tacc_list = transpose(tacc_list)
old_tacclist = cat(1,tacc_list,0);
ref_assign_list(1:ctr+1,1) = 1;
ref_assign_list(ctr+1,1) = NaN;

T = table(final_filename_list,old_tacclist,ref_assign_list);

data_filename = strcat(new_filename,'File_List.csv');
writetable(T,data_filename,'WriteVariableNames',false)
```